Article

Fabrication of a Dual-Targeted Liposome-Coated Mesoporous Silica Core−Shell Nanoassembly for Targeted Cancer Therapy

Kavini Rathnayake, Unnati Patel,* Emily C. Hunt, and Nirupama Singh

Cite This: *ACS Omega* 2023, 8, 34481−34498

Read Online

ACCESS | Metrics & More | Article Recommendations | Supporting Information

ABSTRACT: Nanoparticles have been suggested as drug-delivery systems for chemotherapeutic drugs to allow for controlled drug release profiles and selectivity to target cancer cells. In addition, nanoparticles can be used for the in situ generation and amplification of reactive oxygen species (ROS), which have been shown to be a promising strategy for cancer treatment. Thus, a targeted nanoscale drug-delivery platform could be used to synergistically improve cancer treatment by the action of chemotherapeutic drugs and ROS generation. Herein, we propose a promising chemotherapy strategy where the drug-loaded nanoparticles generate high doses of ROS together with the loaded ROS-generating chemotherapeutic drugs, which can damage the mitochondria and activate cell death, potentiating the therapeutic outcome in cancer therapy. In the present study, we have developed a dual-targeted drug-delivery nanoassembly consisting of a mesoporous silica core loaded with the chemotherapeutic, ROS-generating drug, paclitaxel (Px), and coated

with a liposome layer for controlled drug release. Two different lung cancer-targeting ligands, folic acid and peptide GE11, were used to target the overexpressed nonsmall lung cancer receptors to create the final nanoassembly (MSN@Px) L-GF. Upon endocytosis by the cancer cells, the liposome layer was degraded by the intracellular lipases, and the drug was rapidly released at a rate of 65% within the first 20 h. In vitro studies confirmed that this nanoassembly was 8-fold more effective in cancer therapy compared to the free drug Px.
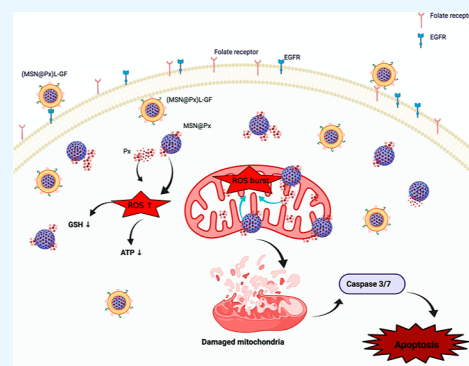
INTRODUCTION

Cancer is a major global health concern with a global incidence rate of nearly 18.1 million new cases per year.[1] According to the American Lung Cancer Association, 154,050 Americans are expected to die from lung cancers each year.[2] The growing incidence of cancer causes a significant healthcare burden, with initial treatments costing upward of 20,000 USD.[3] Hence, it is imperative to explore more treatment options that increase cancer survivorship and are cost-effective. Current treatments for cancer include surgery, radiation therapy, immunotherapy, and chemotherapy.[4] Chemotherapy remains one of the most common methods of cancer treatment despite its limitations. The shortcomings of the chemotherapeutic drugs include not only their severe side effects but also many characteristics of the chemotherapeutic drugs, such as their lack of water solubility, low circulation time in the bloodstream, and inability to directly target the cancer cells.[5] Nanotechnology-based approaches of drug delivery offer solutions to these problems through their tunable properties.[5−7] Nanoparticles can be designed as drug-delivery systems that increase the solubility and the circulation time of the chemotherapeutic drugs, and additionally, nanoparticle therapies can incorporate ligands that allow for precise targeting of the cancer cells.[6,8]

Reactive oxygen species (ROS) are reactive chemical species that act as a redox signaling messenger for many normal physiological functions of the cells, such as cellular proliferation, differentiation, and migration.[9,10] Furthermore, excessive amounts of ROS can damage lipids, proteins, and DNA, which is associated with changes of mitochondrial functions.[10] It has been reported that some drugs and nanoparticles can induce ROS inside cells.[11] Therefore, loading an ROS-generating chemotherapeutic drug inside mesoporous nanoparticles will synergistically induce an ROS burst, leading to cell death in the cancer cells.

Mesoporous silica nanoparticles (MSNs) have been suggested as drug-delivery vehicles due to their large surface area and porous structure, which make them ideal carriers for various pharmaceuticals and biological molecules.[12−14] MSNs have many advantages over other nanomaterials, such as their stability under biological conditions, biocompatibility, and capability to be loaded with both hydrophilic and hydrophobic drugs.[15] MSNs can also be modified with stimuli-responsive groups to achieve controlled drug delivery.[16] Due to their unique structural properties and capacity for modification with

a variety of functional groups, MSNs have been suggested as drug-delivery systems for chemotherapeutic drugs.[17] Paclitaxel (Px), sold under the brand name Taxol, is a chemotherapeutic drug that promotes the polymerization of tubulin to form microtubules and directly inhibits the disassembly of microtubules, causing cell death by interfering with the normal microtubule dynamics that are required for cell division.[18,19] It is reported that a 3-weekly Px schedule is the most common regimen for the treatment of advanced nonsmall cell lung cancer cells.[20] Additionally, Px has been shown to promote the generation of the ROS, which can lethally damage the nearby cancer cells that have not been exposed to Px.[21] Hence, cancer cell survival critically depends upon the ROS levels, which at low concentration can increase tumorigenesis but at high concentration increases apoptosis.[22] Due to its effectiveness against a wide range of cancers, chemotherapy with Px has become a common treatment for cancer, despite its disadvantages, namely, its insolubility in water and its toxicity at high doses.[19,23]

Nanoparticles have previously been shown to be effective drug-delivery platforms for Px, with some formulations used in clinical trials.[23] The previous formulations of nanoparticle carriers for Px have been mostly polymer-based[24,25] or lipid-based.[26] However, recently, inorganic nanoparticles have drawn increased interest as carriers for Px for their various unique properties. MSNs, in particular, have been suggested as the ideal carrier systems for Px due to their low toxicity and their ability to increase the solubility and adsorption of Px.[27,28] Furthermore, the release of Px from the MSNs can be controlled by tailoring the pore size of the nanoparticles or by coating the MSNs with a protective liposome layer, which controls the drug release through the gatekeeping action of the lipid layer.[13,29,30] MSNs have also shown effective coloading of Px and other chemotherapeutic agents, which reduces the chances of drug resistance.[30,31] Yan et al. have reported Px and doxorubicin-coloaded mesoporous nanoparticles for chemotherapy.[32] Coating the Px-loaded MSNs with a liposome layer further facilitates the attachment of the targeting ligands for specific cell recognition and improves biocompatibility. This drug-delivery strategy is designed to reduce the lethality of high doses of chemotherapeutic drugs required in the treatment and the incidence of multidrug resistance. Hence, we developed a nanoassembly that simultaneously acts as a controlled and targeted drug-delivery vehicle, which effectively inhibits lung cancer cells compared to that by free Px itself. The mechanism of Px-related cell death in the nanoassembly was further studied.

Herein, we report the synthesis of MSNs loaded with Px and further coated with a liposome (L) layer, which acts as a gate keeper for drug release. The nanoassembly was further functionalized with a folate receptor-targeting folic acid (FA) and epidermal growth factor receptor (EGFR)-targeting peptide (GE11) as a dual target to create the final nanoassembly, (MSN@Px) L-GF.[14,25,33−35] These receptors are popular biomarkers of cancerous cells.[36,37] Furthermore, this nanoassembly was used to study the mechanistic effects of ROS-induced lung cancer cell death with (MSN@Px) L-GF compared to that with free Px. Px was rapidly released from the nanoassembly through the degradation of the liposome layer triggered by the intracellular lipases. The release of Px leads to enhanced ROS generation and oxidative stress, which lead to mitochondrial dysfunction and ultimately induce apoptosis through caspase activation. It has been found that this

nanoassembly has an 8-fold increase in effectiveness compared to that of the free drug Px. This versatile nanocomposite-promoted therapeutic efficacy through controlled release of the chemotherapeutic drug at the targeted cancer cells with negligible systemic toxicity makes it a potent candidate for enhancing tumor suppression while reducing the incidences of multidrug resistance.

■ MATERIALS AND METHODS

Cetyltrimethylammonium bromide (CTAB, >99%), tetraethyl orthosilicate (TEOS, 98%), phosphate-buffered saline (PBS, 0.5×), ammonium hydroxide (NH$_4$OH, 25%), hydrochloric acid (HCl, >99%), sulfo-N-hydroxysuccinimide (sulfo-NHS, 99%), wortmannin, chlorpromazine, nystatin, folic acid, and rhodamine B isothiocyanate (RITC) were purchased from Sigma-Aldrich (St. Louis). 1,2-Dipalmitoyl-sn-glycero-3-phosphocholine (DPPC), 1,2-dioleoyl-sn-glycero-3-phosphoethanolamine (DOPE), cholesterol (ovine), 1,2-distearoyl-sn-glycero-3-phosphoethanolamine-N-[amino(polyethylene glycol)-2000] (ammonium salt) [DSPE-PEG(2000) amine], and the mini-extruder kit were purchased from Avanti Polar Lipids (Alabama). 1-Ethyl-3-(3-(dimethylamino)propyl)-carbodiimide (EDC) was obtained from Alfa Aesar. GE11 peptide (Tyr-His-Trp-Tyr-Gly-Tyr-Thr-Pro-Gln-Asn-Val-Ile) was obtained from Phoenix Pharmaceuticals Inc. (California). A549 lung cancer cells were purchased from the American Type Culture Collection (ATCC, CCL-185) (Virginia). The CellEvent caspase 3/7 green detection reagent, live/dead viability kit, MitoProbe JC-1 assay kit, Tubulin Tracker, Green detection kit, micro-BCA protein assay kit, and Scientific and Invitrogen ATP Determination kits were purchased from Thermo Fisher Scientific (Massachusetts). The fluorometric intercellular ROS kit was purchased from Sigma-Aldrich (Missouri). The GSH-Glo Glutathione assay was purchased from Promega Corporation (Wisconsin). (3-(4,5-Dimethylthiazol-2-yl)-2,5-diphenyltetrazolium bromide) (MTT) cell proliferation kit, Hoechst, 4′,6-diamidino-2-phenylindole (DAPI), and calcein AM were purchased from Thermo Fisher Scientific (Massachusetts). Ham's F-12K nutrient mixture with L-glutamine (F-12K, 1×), fetal bovine serum (FBS, 10%), trypsin EDTA (2.21 mM), and penicillin−streptomycin (Pen-Strep), 1× were obtained from Corning (New York). The particle hydrodynamic diameter was evaluated by dynamic light scattering (DLS) using a Malvern Zetasizer (Malvern Panalytical Inc., Massachusetts). Nitrogen adsorption−desorption was performed using an Autosorb iQ-C-MP/XR surface area and porosity analyzer (Quantachrome Instruments, Florida). Thermogravimetric analyses were performed on a Discovery Q550 (TA Instruments, Massachusetts). The absorbance and fluorescence measurements were recorded with a SpectraMax M2 multimode microplate reader (Molecular Devices, California). Drug-release studies were conducted using high-performance liquid chromatography (HPLC) using a Hitachi Primaide Separation module and a 1430 diode array detector.[38] Fluorescence microscopy images were recorded by a CKX53 inverted fluorescence microscope (Olympus, Pennsylvania). The transmission electron microscopy (TEM) images were recorded by an FEI Tecnai Osiris operating at 200 kV (SelectScience, UK). The Fourier transform infrared (FT-IR) spectra were recorded with a Nicolet iS50 attenuated total reflection Fourier transform infrared spectrometer(Thermo Fisher Scientific, Massachusetts). The mammalian cells were grown in a CO$_2$ incubator,

and PA14 was cultured in a class II biological safety cabinet (Thermo Fisher Scientific, Massachusetts). Sterile medium, sterile glassware, and sterile disposables were used for all experiments. Unless specifically mentioned otherwise, all media and glassware were sterilized using a Benchmark benchtop liquid sterilizer (BioClaveTN, New York). The viable bacteria count was determined from a CytoSMART automated cell counter (Corning, New York).

Synthesis of the MSNs. The MSNs were prepared using a previously reported protocol with some modifications, using CTAB as the porous template.[13] TEOS is used as the silica source. CTAB (4 mmol) was dissolved in 140 mL of water, and TEOS (1688 μL, 7.6 mmol) was added dropwise to the mixture. NH$_4$OH (25 v/v %, 1688 μL) was then added to the mixture and stirred overnight at room temperature. On the following day, the white turbid solution was separated by centrifugation at 12,000 rpm for 10 min. After removing the supernatant, the solid precipitate (MSNs) was resuspended in water and centrifuged at 12,000 rpm for 10 min. This was repeated three times. To remove the excess CTAB, the MSNs were centrifuged and resuspended in 50 mL of ethanol and 200 μL of concentrated HCl. This mixture was stirred at 60 °C for 12 h. The resulting product was purified three times with ethanol by centrifuging at 12,000 rpm for 10 min. The sizes of the MSNs were characterized through DLS and TEM.

Px Encapsulation in MSNs (MSN@Px). MSNs (5 mg/mL) were loaded with Px (10 μg) in 5 mL of DMSO. This was stirred overnight at 37 °C. The unconjugated Px was removed by centrifugation at 12,000 rpm for 10 min, yielding MSN@Px.

Liposome Preparation. Liposomes were prepared as described by Rathnayake et al. with minor modifications.[13] Briefly, DPPC (15 mg, 20 μmol), DOPE (1.25 mg, 1.7 μmol), cholesterol (7.5 mg, 3.2 μmol), and DSPE-PEG(2000) amine (1.25 mg, 0.45 μmol) were dissolved in 3 mL of chloroform and evaporated in a rotary evaporator, which yielded a thin lipid film. The lipid film was rehydrated in 2.5 mL of PBS (pH 7.4) at a lipid concentration of 10 mg/mL and extruded 15 times through a polycarbonate membrane (pore size 400 nm) using the mini extruder. The resultant liposomes were stored at 4 °C for further use.

Modification of Liposomes with GE11 and FA. GE11 and FA were conjugated to the exterior of the liposomes by EDC activation chemistry. GE11 (100 μg) and FA (30 μg) at a molar ratio of 90:10 were activated with EDC (3.29 μmol) and sulfo-NHS (8.24 μmol) for 2 h at 37 °C. Thereafter, the liposomes containing DSPE-PEG(2000) amine (1.25 mg, 0.45 μmol) were added to the activated GE11 and FA mixture and incubated overnight at 37 °C. At the end of the incubation period, the GE11- and FA-modified liposomes were purified by centrifugation at 12,000 rpm for 30 min at 4 °C and resuspended in PBS (pH 7.4). The purified product was lyophilized and stored at −20 °C until further use. The amount of conjugated FA was determined by analyzing the supernatant after conjugation by UV–vis spectroscopy at 310 nm. Also, the conjugated GE11 was assessed using micro-BCA protein assay (Supporting Information Figure S4).

Encapsulation of MSN@Px into the Liposomes ((MSN@Px) L). To prepare liposome-coated MSN@Px, 25 mg of MSN@Px was resuspended in the liposomes (2 mL, 25 mg/mL) in PBS and mixed for 20 min on ice. The liposome-coated nanoassembly (MSN@Px) L was separated from the empty liposomes by centrifugation at 12,000 rpm for 5 min

and repeatedly washed in PBS. The resultant (MSN@Px) L was lyophilized and dried at −20 °C until further use.

Characterization through TEM and DLS. The ultra-structure of bare MSNs, MSN@Px, and (MSN@Px) L was examined through TEM. Carbon thin-film-coated Cu grids (200 mesh) were drop-cast using a diluted solution (100 μL, 5 mg/mL) of the material and left to vacuum-dry overnight. The nanoassemblies were visualized using a transmission electron microscope operating at 200 kV. The liposomal layer was examined through TEM following staining with 10% uranyl acetate. The hydrodynamic size and zeta potential were measured using DLS.

Surface Area and Pore Volume Determination of the MSNs and MSN@Px. The surface areas of the MSNs and MSN@Px were determined using the Brunauer−Emmett−Teller (BET) method using a surface area and porosity analyzer. The cumulative pore volume was calculated from the adsorption branch of the isotherm using the Barrette−Joyner−Halenda (BJH) model.

TGA of the Px Content in MSN@Px and (MSN@Px) L-GF. Thermogravimetric analysis (TGA) was carried out under an argon atmosphere (99.999%) where dried MSN@Px (ca. 1 mg) was heated at a rate of 5 °C/min up to 100 °C and then kept isothermal for 15 min followed by a 5 °C/min ramp up to 700 °C. The amount of Px encapsulated in MSN@Px was calculated by analyzing the percentage weight loss difference between MSN and MSN@Px.

Stability of the Nanoparticles. The stability of the (MSN@Px) L-GF was evaluated by monitoring the changes in particle size, zeta potential, and turbidity in a cell culture medium. (MSN@Px) L-GF (5 mL, 10 μg/mL) was kept in the cell culture medium for 5 days at 37 °C to mimic the static conditions for in vitro experiments. The particle size and zeta potential were determined using DLS at the same time on all the 5 days.

Px-Release Studies from (MSN@Px) L-GF. 5 mL of (MSN@Px) L-GF (5 mg/mL) was dispersed in 10 mL of PBS buffer containing 0.1% Tween 80 at pH 5.5 and pH 7.4 and incubated while being shaken at 200 rpm at 37 °C. An aliquot of 1 mL of solution was withdrawn at predetermined time intervals and replaced with an equivalent amount of fresh medium. The removed sample was then centrifuged at 10,000 rpm for 10 min. Following that, the pellet was resuspended in fresh PBS buffer containing 0.1% Tween 80 at respective pH values (pH 5.5 and pH 7.4). Then, the sample was filtered through a 0.5 μm nylon syringe filter. The release profile of Px from (MSN@Px) L-GF was observed through reverse-phase [Welch C-18 column; dimensions 4.6 mm, 200 mm; and particle size (dp): 5 μm] HPLC. The mobile phase consisted of a mixture of acetonitrile and HPLC-grade water (W) containing 0.1% trifluoroacetic acid (TFA) in a ratio of 70:30. The pH of the mobile phase was adjusted to 5 with acetic acid and filtered through a 0.22 mm nylon filter. The HPLC measurements were carried out in an isocratic mode. The injection volume was 20 mL with a flow rate of 1 mL/min. The column temperature was maintained at 25 °C, and elution absorbance was monitored at 227 nm using a photo diode array detector. The released Px concentrations were quantified by preparing a standard calibration curve. The drug-loading capacity (DLC) and encapsulation efficiency (EE) of Px in (MSN@Px) L-GF were also determined through HPLC.

The percentages of DLC and EE of Px were calculated according to the following formula

$$EE\ \% = \frac{\text{total mass of drug added} - \text{mass of unencapsulated drug}}{\text{total mass of drug added}} 100$$

$$DLC\ \% = \frac{\text{total mass of drug added} - \text{mass of unencapsulated drug}}{\text{total mass of MSNs}} 100$$

A549 Cell Proliferation. A549 cells were grown in T75 flasks in a complete growth medium. The complete growth medium was prepared by mixing Ham's F-12K nutrient mixture with L-glutamine (F-12K) (445 mL), FBS (10%, 50 mL), and Pen-Strep (5 mL) followed by sterile filtration. The cells were grown in 20 mL of fresh and prewarmed medium at 37 °C in a humidified atmosphere of 5% CO_2. Cell viability was assessed by the Trypan blue assay, and the cells were counted using an automatic cell counter.

In Vitro Cellular Uptake. A549 cells were seeded on 24-well plates (10^3 cells per well) for 24 h. The cells were cocultured with RITC-conjugated MSNs, MSN@Px, (MSN@Px) L, or (MSN@Px) L-GF containing the encapsulated Px equivalent of 10 μg/mL for 6 h. Thereafter, the cells were washed with PBS three times. The nuclei were then stained with DAPI (blue) for 10 min and fixed with 4% paraformaldehyde for 30 min and washed with PBS. The cellular uptake ability was examined by an inverted fluorescence microscope.

Cellular Uptake Mechanism of (MSN@Px) L-GF. Red fluorescent dye RITC-labeled MSN@Px and (MSN@Px) L-GF were used to quantify the internalization in the presence of various endocytosis inhibitors. A549 cells (10^3 cells per well) were treated with chlorpromazine (20 μg/mL), nystatin (20 μg/mL), and wortmannin (1 μg/mL) for 1 h prior to the addition of the RITC-labeled nanoassemblies. Following that, the cells were vigorously washed with PBS to remove any free particles, and the cells were stained with calcein AM and DAPI. The cells were then examined by fluorescence microscopy. The fluorescence intensity of the internalized nanoassemblies was measured from a microplate reader at 576 nm.

Determination of Intracellular ROS Levels. Intracellular ROS levels were quantified using a fluorescent probe following the manufacturer's instructions. The A549 cells were seeded into 24-well plates at a density of 10^3 cells per well, incubated overnight, and then treated with the MSNs, MSN@Px,, (MSN@Px) L, or (MSN@Px) L-GF (encapsulated Px equivalent to 10 μg/mL) for 4 h. Then, the cells were incubated with the ROS detection reagent for 1 h at 37 °C and 5% CO_2, and the fluorescence intensity was measured with a λ_{ex} of 490 nm and a λ_{em} of 520 nm using the microplate reader.

Mitochondrial Membrane Potential Assay. The JC-1 probe was employed to evaluate the mitochondrial depolarization in the A549 cells. Briefly, the cells were cultured in a 24-well plate with a cell density of 10^3 cells per well and then incubated for 24 h. Following that, the cells were washed with PBS and treated with MSNs, MSN@Px, (MSN@Px) L, (MSN@Px) L-GF, or the free drug Px at a Px equivalent of 10 μg/mL for about 6 h. The cells were washed, treated with an equal volume of serum-free medium containing JC-1 dye (5 mg/L), and incubated at 37 °C for 20 min. This was again rinsed twice with PBS and then replaced with fresh medium without serum. Finally, the fluorescent images were taken using an inverted fluorescent microscope. The images were obtained at 488 nm excitation and 530 nm emission to visualize the green JC-1 monomers and 543 and 590 nm excitation for the red fluorescent JC-1 aggregates.

Intracellular GSH Measurement. The levels of intracellular reduced glutathione (GSH) were quantified using a luciferin derivative. Briefly, the A549 cells were seeded on 24-well plates (10^3 cells per well) overnight and were incubated with 25 μL of different nanoassemblies [MSNs, MSN@Px, (MSN@Px) L, and (MSN@Px) L-GF] or free drug Px having a Px concentration equivalent to 10 μg/mL for 4 h. Following that, the cells were washed with PBS three times and incubated with the GSH-Glo reagent and luciferin detection agent for 30 and 15 min, respectively, according to the manufacturer's instructions. The luminescence intensity was measured after 15 min at 37 °C from a microplate reader. The intracellular GSH levels were expressed in μM and were calculated based on the calibration curve.

Measurement of the Cellular ATP Levels. The intracellular ATP levels were measured using an ATP determination kit. The A549 cells were seeded at a density of 10^3 cells per well and then incubated for 24 h prior to experiments. Then, the cells were treated with MSN@Px, (MSN@Px) L, (MSN@Px) L-GF, or the free drug Px at a Px equivalent to 10 μg/mL for about 6 h in a growth medium supplemented with 10% FBS and 1% pen-strep at 37 °C and 5% CO_2. Thereafter, the cells were washed with PBS and harvested with trypsin EDTA (200 μL) for 5 min at 37 °C. Cold PBS was added to terminate the reaction, and the cells were collected by centrifugation at 10,000 rpm for 10 min. Following that, 30 μL of each sample was mixed with 270 μL of buffer and checked for luminescence. The ATP level was assessed based on the calibration curve.

Caspase Activity Assay. A CellEvent caspase-3/7 assay kit was used to evaluate membrane permeability and caspase activation. The A549 cells (1×10^3 cells/well) were seeded in a 24-well plate, and following 24 h, MSNs, MSN@Px, (MSN@Px) L, (MSN@Px) L-GF, or the free drug Px was added at a Px equivalent to 10 μg/mL and incubated for 6 h. A volume of 100 μL of the caspase 3/7 reagent was added into each well and incubated for 30 min at 37 °C in 5% CO_2 protected from light. The cells were then observed using an inverted fluorescence microscope. Finally, the fluorescence intensity was measured with a micro plate reader using excitation at λ_{ex} 360 nm and λ_{em} 460 nm.

Tubulin Polymerization Fluorescence Assay. The direct effect of the nanoassemblies on tubulin polymerization was determined in a biochemical fluorescence-based detector (Thermo Fisher) according to the manufacturer's protocol. The cells (10^3 cells per well) were incubated with MSNs, MSN@Px, (MSN@Px) L, (MSN@Px) L-GF, or the free drug Px at a Px equivalent to 10 μg/mL for 6 h. The culture medium was removed, washed twice with PBS, and stained with the diluted Tubulin Tracker Green reagent for 30 min at 37 °C and 5% CO_2. The nuclei were stained with DAPI for 15 min. Blue fluorescence (DAPI) and green fluorescence (Tubulin Tracker Green reagent) were observed using a fluorescence microscope.

Live−Dead Assay. A live/dead assay was performed for the analysis of cell viability after the activation of the apoptosis pathways upon the treatment with the synthesized nanoassembly. The cells (1×10^3 cells per well) grown in a 24-well plate were treated with MSNs, MSN@Px, (MSN@Px) L, (MSN@Px) L-GF, or the free drug Px at a Px equivalent to 10 μg/mL for 6 h. Following that, the wells were washed twice with cold PBS and incubated for 30 min with the live/dead reagent (2 μM calcein AM and 4 μM ethidium bromide)

Scheme 1. Synthesis of (MSN@Px) L-GF
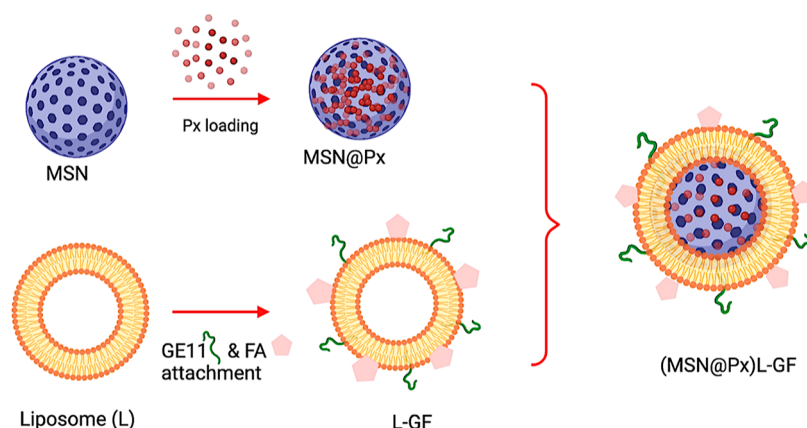
according to the manufacturer's instructions. The samples were washed twice with PBS and imaged by fluorescence microscopy.

In Vitro Cytotoxicity Assays. Mammalian cell viability was evaluated using an MTT assay. The A549 cells were seeded onto 24-well plates at a density of 10^3 cells per well. After 24 h, they were incubated with different nanoassemblies [MSN@Px, (MSN@Px) L, and (MSN@Px) L-GF] and free drug Px having Px concentrations equivalent to 1, 5, 10, 25, 50, or 100 μg/mL for 24 h. Then, 100 μL of the MTT solution (1 mg/mL) was added to each well, and the cells were further incubated for 4 h. Afterward, the culture medium was discarded, and 150 μL of DMSO was added to each well. The absorbance intensity was determined at 540 nm with a microplate reader. The results were presented as the percentage of the viable cells with respect to the untreated control cells.

■ RESULTS AND DISCUSSION

Synthesis and Characterization of the Nanoassemblies. The synthesis of the final nanoassembly is shown in Scheme 1. The MSNs were prepared following the previously reported surfactant-template method.[13] The synthesized MSNs were purified and redispersed in water. The TEM images confirmed the mesoporous structure of the bare MSNs (Figure 1a). The widely used tumor agent, Px, was loaded into the mesoporous particles (see Supporting Information Figure S1 for the Paclitaxel structure). This drug is used in cancer chemotherapy for breast, ovarian, and lung cancers, melanomas, and lymphomas. Px promotes tubulin dimerization and inhibition of the depolymerization of the microtubules, resulting in the formation of abnormally stable and nonfunctional microtubules.[39] Px is incorporated into the pores of MSN using solvent evaporation.[27] Different solvents were utilized to study their drug-loading capacity (see Supporting Information). DMSO was used as the preferred drug-loading solvent as it yielded the highest loading of Px. Px is loaded into the mesoporous nanoparticles via an adsorption mechanism. Px-loaded MSN (MSN@Px) was then encapsulated within a liposome layer (MSN@PX) L. The liposome coating (especially the cholesterol components in the liposome) further prevents the leakage of Px and facilitates Px retention. The liposomes were synthesized via an extrusion method using these phospholipids: DPPC, DOPE, and DSPE-PEG(2000) amine and cholesterol. The prepared MSN@Px was encapsulated within the liposome in a low-temperature ice bath, where

the amphiphilic phospholipids self-assemble around the MSN@Px to create a spherical lipid layer (LL) (Figure 1a). The −NH₂ moieties of the lipid DPPC provide hydrophilicity to the bilayer, which allows the encapsulation of hydrophilic MSNs.[13] The cholesterol in the lipid layer enhances the membrane fluidity and Px retention.[40] The phospholipids, DPPC and DOPE, cause hydrophilicity in the liposome.[41] The large PEG group of the DSPE-PEG(2000) amine is known to reduce immunogenicity and antigenicity and facilitates the targeting peptide binding onto the liposome.[42] The liposome layers act as a gatekeeper and restrict the premature release of Px. The exterior of the liposome was tagged with two different cancer-targeting ligands to enhance the effectiveness of the targeting affinity. FA and the peptide GE11 were conjugated onto the surface of the liposome layer with the help of EDC and sulfo-NHS chemistry (see Supporting Information Figure S2 for FA structure). The folate receptors (such as FR-α) are known to be overexpressed on the surface of the cancer cells with an epithelial origin such as the breast, lungs, and ovary.[36] Therefore, these FRs are commonly used cancer biomarkers.[36] Nonimmunogenicity, stability, tissue permeability, and the ease of bioconjugation chemistry make FA an ideal cancer-targeting agent.[43] FA conjugation facilitates cell internalization through receptor-mediated endocytosis.[44] Using a second targeting moiety such as epidermal growth factor receptor (EGFR) increases the drug carrier's interaction with the cancer cells. GE11 (YHWYGYTPQNVI) is a dodecapeptide that binds specifically to EGFR, which is overexpressed in a number of tumors of epithelial origin, such as the breast, ovary, and lungs.[37] This small peptide is also nonimmunogenic and facilitates good penetration into the tumor tissues. Also, it has been found that GE11 possesses a high potential to accelerate endocytosis through an alternative EGFR-dependent actin-driven pathway.[35] Our study confirms the successful attachment of both the targeting ligands (FA and GE11) on the nanoassembly. (MSN@Px) L-GF was qualitatively characterized by DLS, TEM, and FT-IR and quantitatively by BET and TGA.[45] The synthesis of the nanoassembly was monitored by TEM (Figure 1a). Upon Px loading, there is a clear reduction of porosity of the MSN (Figure 1a). This reduction in porosity was confirmed by BET analysis (see Supporting Information Table S1). Following Px loading, the MSNs were coated with a liposome layer. A single layer of lipids around each MSN@Px is clearly observed as shown in Figure 1a. The size of the nanoassemblies was determined by both DLS and TEM. As shown in Figure 1b, the diameter from TEM was 83 ± 4 nm,
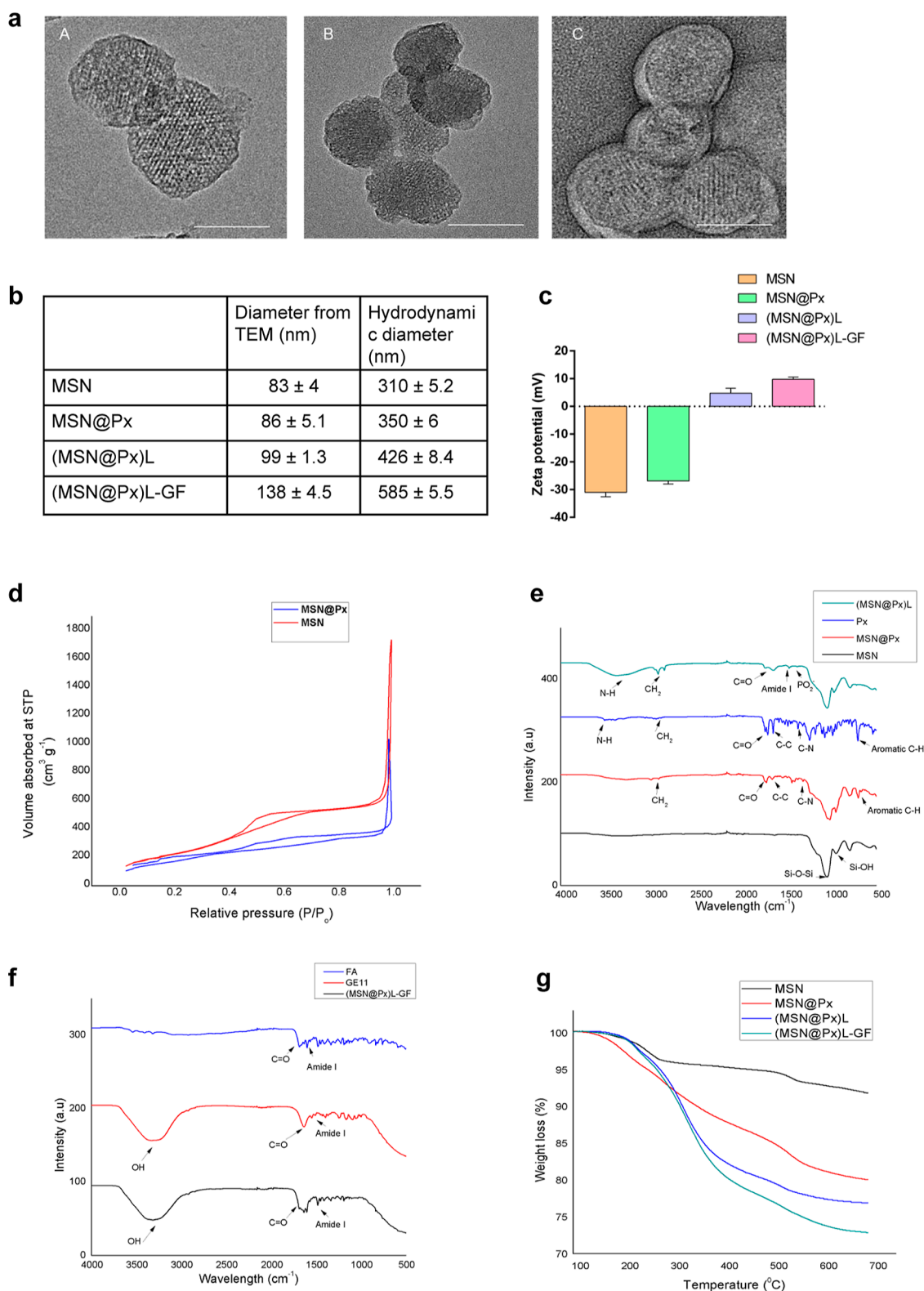
Figure 1. Characterization of the nanoassemblies. (a) TEM image of (A) MSNs, (B) MSN@Px, and (C) (MSN@Px) L (scale bar = 100 nm). (b) Dried (TEM) and hydrodynamic (DLS) size of the nanoassemblies. (c) Zeta potential change in various steps of the synthesis of the nanoassemblies. (d) N_2 adsorption−desorption isotherms for MSNs and MSN@Px. (e) FT-IR spectra of MSNs, MSN@Px, Px, and (MSN@Px) L. (f) FT-IR spectra of dual targets showing FA, GE11, and (MSN@Px) L-GF. (g) TGA curves recorded for MSNs, MSN@Px, (MSN@Px) L, and (MSN@Px) L-GF.

while the hydrodynamic diameter was around 310 ± 5.2 nm. The increased hydrodynamic size measured by the DLS was probably due to particle swelling and agglomeration in the liquid media, where the dried size of one individual particle was measured from the TEM images. Upon liposome coating, the diameter of the MSNs had increased from 83 ± 4 to $99 \pm$
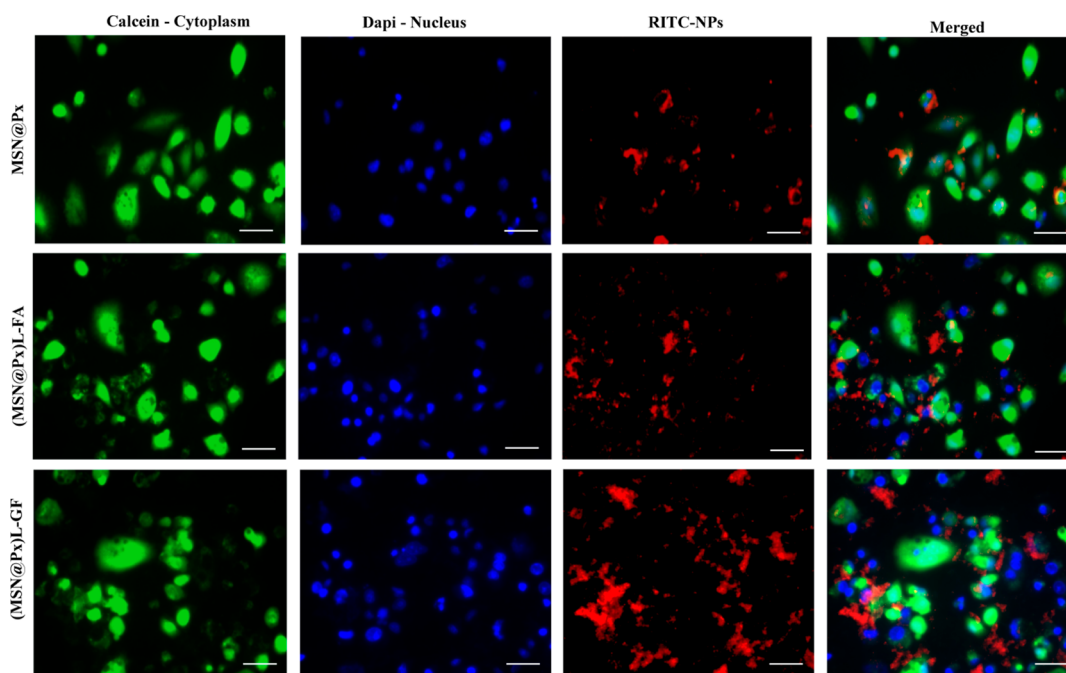
Figure 2. Targeting ability of nontargeted MSN@Px and single-ligand-targeted (MSN@Px) L-FA compared to that of the dual-targeted (MSN@Px) L-GF. The nanoparticles were conjugated with RITC (red), and the A549 cells and the nuclei were stained with calcein AM and DAPI, respectively (scale bar, 50 μm).

1.3 nm, as determined by the TEM analysis. Upon conjugation of the targeting ligands, the size increased further up to 133 ± 4.5 nm (Figure 1b).

The surface electrical potential was determined by measuring the zeta potential in each step to confirm the successful synthesis of the nanoassembly (Figure 1c). The MSNs showed a negative zeta potential (−31 ± 1.6 mV), indicating the presence of negatively charged silicate ions on the surface of MSNs (Figure 1c). With Px loading, the zeta potential was slightly increased to −26.9 ± 1.1 mV, indicating that the Px loading did not affect the surface charge of the MSNs.[46] The zeta potential of the bare liposomes was analyzed before incubation with MSN@Px and ranged from 0 to 6.5 ± 1.1 mV. After incubation with the liposomes, the zeta potential increased to 4.7 ± 1.8 mV in (MSN@Px) L, which confirmed the presence of positively charged phospholipid heads in the liposome layer. With the conjugation of the targeting moieties, the zeta potential of the nanoassembly further increased up to 9.8 ± 0.8 mV. The increase in the positive zeta potential was probably due to the protonation of the amino groups on GE11 (at pH 7.4), increasing the positive charge on the final nanoassembly. Moreover, the isoelectric point (pI) of GE11 was found to be 7.67.[47] This depicts the successful conjugation of FA and GE11 onto the liposome (Figure 1c).[34,48] The change in the porosity of the MSN and MSN@Px was assessed by N$_2$ adsorption−desorption isotherms (Figure 1d). The reduction in the surface area, pore volume, and pore size in Px-loaded MSNs compared to those of the bare MSNs further confirmed the successful Px loading (Supporting Information Table S1).

This depicts the successful conjugation of FA and GE11 onto the liposome (Figure 1c).[34,48] The change in the porosity of the MSN and MSN@Px was assessed by N$_2$ adsorption−desorption isotherms (Figure 1d). The reduction in the surface area, pore volume, and pore size in Px-loaded MSNs compared

to that in the bare MSNs further confirmed successful Px loading (Supporting Information Table S1).

FTIR spectroscopy was conducted after each step in the nanoassembly synthesis to confirm the chemical characteristics of the nanoassembly (Figure 1e). FTIR of MSN displayed a characteristic absorption peak at 1020−1110 cm^{-1}, which can be assigned to the Si−O−Si bending and the Si−OH stretching vibration, and a peak at 960 cm^{-1}, indicative of the asymmetric bending.[13] FTIR analysis was also used to confirm the removal of toxic CTAB during the MSN purification. The spectrum of CTAB was compared to the spectrum of MSN, demonstrating the successful elimination of CTAB during MSN synthesis (see Figure S7 of the Supporting Information). Upon Px loading, the MSN@Px FTIR spectrum indicated the corresponding Px peaks.[27] The asymmetric and symmetric stretching vibrations of the CH$_2$ groups can be seen at 2976−2885 cm^{-1}. The peak at 1734 cm^{-1} corresponds to the C=O stretching vibrations of the ester groups. Furthermore, the C−N stretching vibration is located at 1276 cm^{-1}. The absorption peaks at 1647 and 709 cm^{-1} are associated with the aromatic bonds.[49,50] The liposome layer on (MSN@Px) L was identified by the presence of very strong peaks at 2918 and 2850 cm^{-1} corresponding to the antisymmetric and symmetric C−H stretching, respectively, in the long carbon chains of the lipids used.[51] Also, the C=O stretching vibration around 1735 cm^{-1} and the PO$_2^{-1}$ symmetric stretching vibration around 1090 cm^{-1} are from the phospholipids, confirming the successful liposome coating.[13] The specific C=O absorption at 1500 cm^{-1} in (MSN@Px) L-GF was similar to the C=O absorption of GE11, indicating the presence of GE11.[52] The characteristic IR absorption peaks of FA can be seen at 1605, 1693, and 1485 cm^{-1} which correspond to the amide N−H bending, the C=O stretching of the α-carboxyl group, and the absorption band of the phenyl ring, respectively, and are also represented in (MSN@Px) L-GF. Furthermore, the FTIR spectra of (MSN@
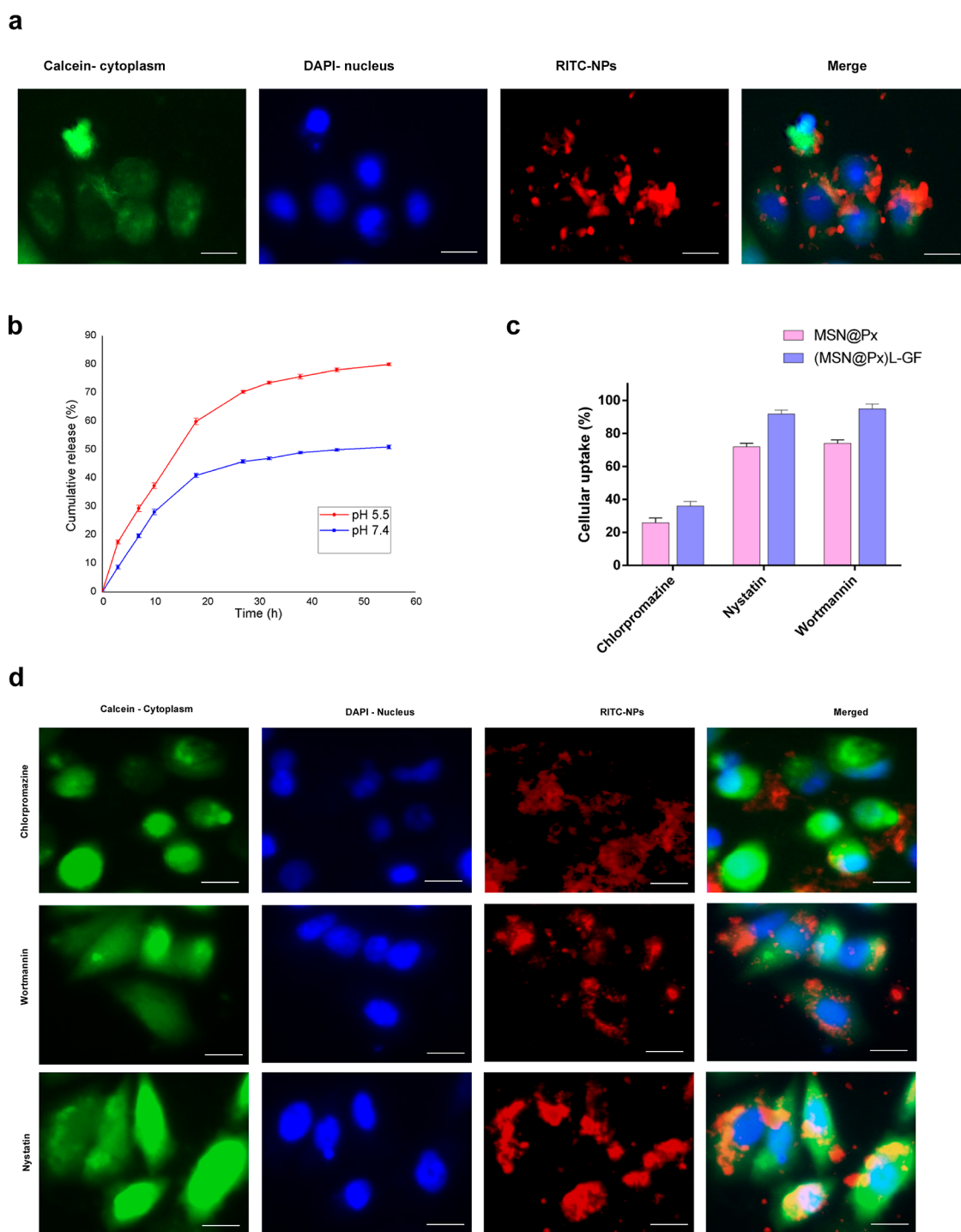
Figure 3. Evaluation of the nanoparticle internalization and drug-release profiles. (a) Internalization of (MSN@Px) L-GF into the A549 cells. (b) Cumulative release of Px from (MSN@Px) L-GF at pH 5.5 and pH 7.4. (c) Percentage of (MSN@Px) L-GF cytoplasmic delivery after treatment with various inhibitors. (d) Fluorescence microscopy images of the A549 cells treated with various inhibitors showing the difference in cellular internalization (scale bar, 100 μm).

Px) L-GF showed an intense broad peak at 1650 cm^{-1} (Figure 1f), which can be attributed to the new carbonyl (C=O) stretching of amide I absorption of the newly formed amide bond with the NH$_2$ of the liposomes and COOH of FA and GE11.[33,53]

Quantitative ligand analysis of the nanoassembly after each step of synthesis was performed using TGA (Figure 1g). Percentage (%) weight loss at each step was calculated to determine the amount of ligand conjugated. The Px loading in

the MSNs was found to be 98 ± 1.9 mg/g of MSNs, which corresponds to 9 ± 0.5% loading. Also, the percentage weight loss between (MSN@Px) L and MSN@Px indicated that the coated lipid layer constituted 6 ± 0.8% of (MSN@Px) L. The TGA analysis results of (MSN@PX) L-GF and (MSN@Px) L revealed a total percentage weight loss of 4 ± 0.4%, indicating that the total targeting ligand (GE11 and FA) content was 38 ± 4 μg/g in (MSN@Px) Ln (Figure 1g). The FA quantification using the absorbance assay provided a value of
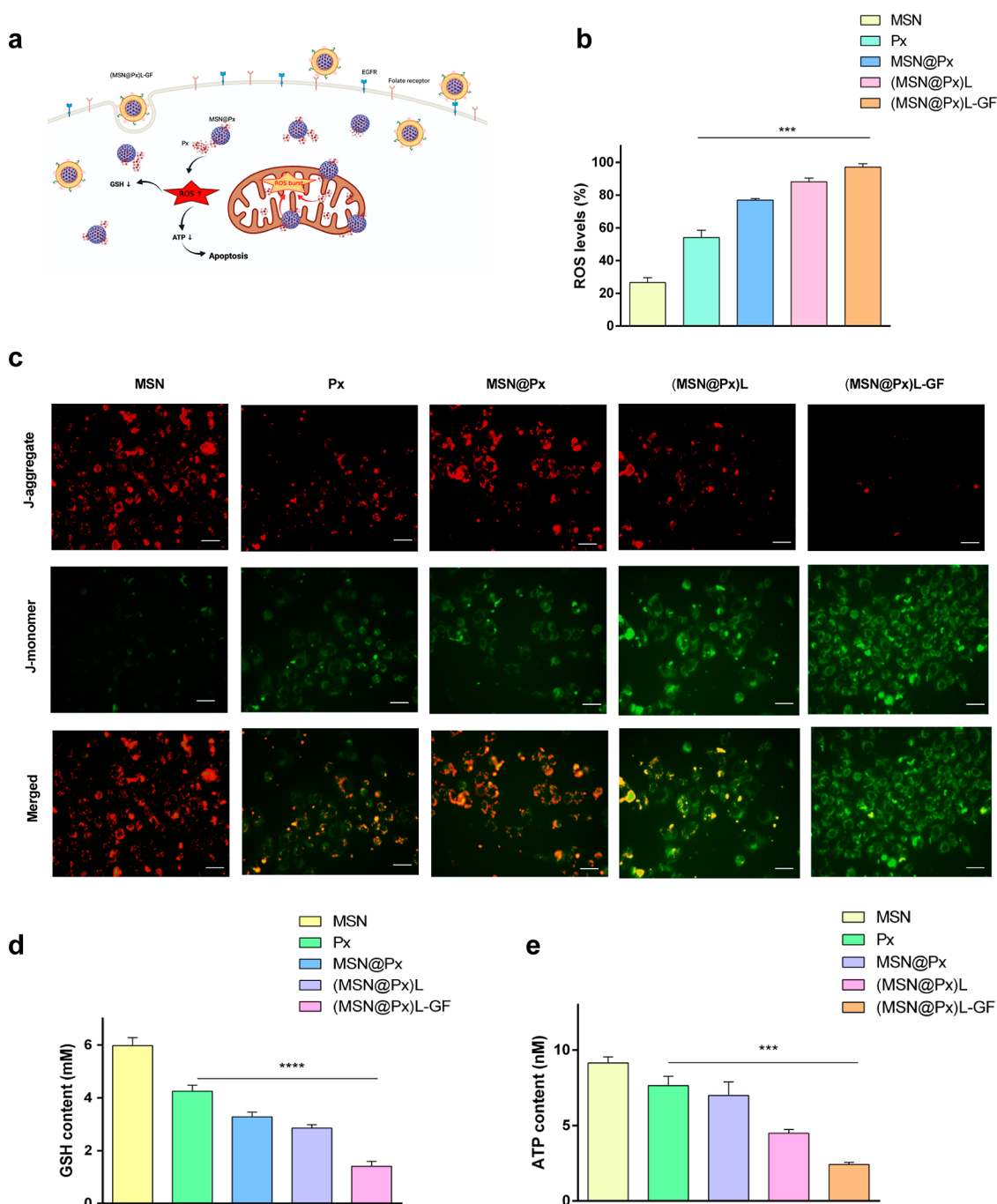
Figure 4. Mitochondrial damage-induced apoptosis of the A549 cells by (MSN@Px) L-GF. (a) Schematic showing the relationship among ROS, GSH, and ATP levels upon (MSN@Px) L-GF endocytosis by the cancer cells and (b) production of intercellular ROS upon nanoassembly internalization. Data are presented as the mean ± SD ($n = 3$, *** indicates $p < 0.001$). (c) Fluorescence microscopy images of JC-1-stained A549 cells after different nanoassembly treatments. The fluorescence transition from red (live) to green (dead) indicates significant mitochondrial damage (scale bar, 20 μm). (d) Cellular GSH level after treatment with different nanoassemblies. Data are presented as the mean ± SD ($n = 3$, **** indicates $p < 0.0001$). (e) Concentration of the ATP after treatment with different nanoassemblies. Data are presented as mean ± SD ($n = 3$, *** indicates $p < 0.001$).

20 μg/g (see Supporting Information Figure S3 for the FA calibration curve). Hence, the GE11 content can be assumed to be 18 μg/g (see Supporting Information Figure S4 for the GE11 calibration curve).

The stability of the nanoparticles is crucial as it impacts essential qualities required for their therapeutic applications, such as long-term storage stability, prolonged biological activities at the tumor site, and circulation in body.[54] The

liposomal coating affords stability to the nanoparticles. The stability of (MSN@Px) L was tested against the uncoated nanoparticles of MSN@Px (Supporting Information Figure S8) by monitoring the changes in size, zeta potential, and turbidity of the particles in the A549 growth medium. The results confirmed that the zeta potential and the size were quite stable in the liposome-coated particles compared to those in the uncoated particles throughout the 5 days at 37 °C under

pH 7.4 (SI). (MSN@Px) L with a positive surface charge might bind strongly to the negatively charged cancer cell membrane by electrostatic interaction and facilitate a high cellular uptake and high stability.[55]

EE and DLC are two important parameters in determining the drug release. EE and DLC were quantified by RP-HPLC. EE % was calculated to be 89.4 ± 1.2% and 85. 2 ±3.5% for MSN@Px and (MSN@Px) L-GF, respectively, which was conducive to drug delivery. The DLC was calculated to be 27.8 ± 3.2 and 24.5 ± 2.1% for MSN@Px and (MSN@Px) L-GF, respectively. The targeting affinity of the nanoassemblies was further determined using fluorescence microscopy (Figure 2). The higher red fluorescence was present with (MSN@Px) L-GF when compared to that with the single-ligand-targeted (MSN@Px) L-FA and nontargeted MSN@Px confirmed a higher internalization, which is possibly due to the addition of both the targeting ligands, FA and GE11.

Cellular Uptake and Drug Release. The cellular uptake and intracellular distribution of the nanoparticles were further studied by fluorescence microscopy (Figure 3a). After 6 h of treatment with RITC-conjugated (MSN@Px) L-GF, the internalization of particles was observed through fluorescence microscopy (Figure 3a). As shown in Figure 3a, there is an increase in the red fluorescence surrounding the DAPI-stained nucleus, confirming that (MSN@Px) L-GF internalized into the cells. This will ultimately enhance the satisfactory therapeutic results.

The in vitro drug-release profiles of Px from (MSN@Px) L-GF were determined using RP-HPLC analysis at pH 5.5 and 7.4, as shown in Figure 3b. The cumulative Px release at pH 5.5 was remarkably higher than that at pH 7.4. The release of Px was affected by the pH, which can be attributed to the acid-catalyzed dissociation of the hydrophobic interactions of Px within the mesoporous core.[54,56] The pH of the extracellular tumor environment (6.5−6.8) tends to be more acidic than that of the normal tissues and further decreases to 4.5−5 in the lysosomes and 5.5−6.0 in the endosomes.[57] In addition, (MSN@Px) L-GF presented a rapid release (65%) in the first 20 h at pH 5.5 compared to that at pH 7.4 (40%) at the same time period. After around 55 h, the release at pH 5.5 reached more than 80% (Figure 3b). This confirms that (MSN@Px) L-GF exhibits a pH-dependent and rapid drug release in the acidic tumor microenvironment. Furthermore, degradation of the liposome layer can be attributed by the intracellular enzymes, such as lipases, upon endocytosis into the cancer cells.[58]

To understand the mechanistic pathway of cellular internalization, an endocytosis inhibitor study was conducted. A549 was treated with a clathrin-mediated endocytosis inhibitor—chlorpromazine (Cpz), caveolin-medicated endocytosis inhibitor—nystatin (Nys), or macropinocytosis inhibitor—wortmannin (Wort) for 1 h prior to the addition of RITC-labeled (MSN@Px) L-GF.[59] After incubation for 6 h, the cells were vigorously washed to remove the free particles and then examined by fluorescence microscopy and quantified using the fluorescence intensity from a spectrophotometric plate reader. The quantitative analysis results confirmed a significant reduction in uptake in the presence of Cpz compared to that in both Nys and Wort (Figure 3c,d). Therefore, it is possible that the internalization mechanism occurs through a clathrin-mediated pathway.

Intracellular ROS, Mitochondria Damage, GSH, and ATP. ROS are generated as a result of the reduction of oxygen

during aerobic respiration and by various enzymatic systems within the cell.[60] It has been reported that the nanoparticle-induced toxicity will lead to ROS generation and consequent oxidative stress.[61] The physiological levels of ROS mediate crucial intracellular signaling pathways and are essential for cell survival. However, excess of ROS formation generates cell damage and death.[62] Hence, the production and role of ROS in apoptosis were investigated (Figure 4a).

Once the (MSN@Px) L-GF nanoassemblies are internalized, the intracellular enzymes will degrade the protective lipid layer and permit the release of Px.[63] The release of Px following the internalization of the nanoassemblies produces ROS, such as intracellular O_2^{-1} and H_2O_2.[64] These ROS cause mitochondrial membrane depolarization, impair the ability of mitochondria to synthesize ATP, and cause DNA damage and cell membrane destruction, which ultimately result in apoptosis.[65] The production of ROS was determined using an ROS-specific dye, H_2DCFDA. Following 1 h of incubation, H_2DCFDA penetrates the cellular membrane and is enzymatically cleaved by esterase. Upon deacetylation, H_2DCFDA is converted into nonfluorescent H_2DCF, which is then rapidly oxidized to highly fluorescent 2′,7′-dichlorofluorescein (DCF) in the presence of ROS and can be detected by the plate reader at 520 nm (Figure 4b).[66] As shown in Figure 4b, the ROS levels increase with each nanoassembly from MSNs to (MSN@Px) L-GF. This confirms that as more particles are internalized and more Px is released inside the cells, the levels of ROS inside the cells increase.

The intrinsic apoptotic pathway is mainly activated by an ROS burst, which induces the opening of the mitochondrial permeability transition pore, which may cause the release of the proapoptotic molecules, such as cytochrome *c*—an intermembrane space protein, to the cytosol.[67] The mitochondrial release of cytochrome *c* is required for caspase activation and mitochondrial membrane depolarization, which further leads to the apoptosis of the cells.[10] The nanoassemblies were investigated for excessive ROS-induced mitochondrial dysfunction by evaluating the mitochondrial membrane potential using JC-1 staining (Figure 4c).[10] JC-1 dye has long been used to examine the mitochondrial status in apoptosis studies.[68] The green fluorescent monomer of JC-1 can enter the cytoplasm and aggregate in normal mitochondria, forming the red fluorescent J-aggregate, which emits orange-red fluorescence with a maximum at 595 nm.[68] Hence, the fluorescence transition from red to green suggests a loss of membrane potential and significant mitochondrial damage (Figure 4c). After 12 h of exposure to (MSN@Px) L and (MSN@Px) L-GF, the appearance of the green fluorescence indicates damaged mitochondria (Figure 4c). These data indicated a considerable mitochondrial dysfunction, which ultimately leads to the development of apoptosis.

The change in the intracellular reduced GSH levels is also an important test of the mitochondrial dysfunction since reduced GSH is an indicator of oxidative stress in a toxicological response that leads to apoptosis.[69] Oxidative stress refers to the elevated intracellular levels of ROS.[70] Among the enzymatic systems involved in the maintenance of the intracellular redox balance, a main role is played by GSH as a nonenzymatic antioxidant that maintains healthy levels of ROS.[71] Hence, the levels of intracellular GSH were quantified using the GSH-Glo glutathione assay, which involves a luciferin derivative that is capable of conversion into luciferin in the presence of GSH (Figure 4d). This assay was used to determine the GSH levels
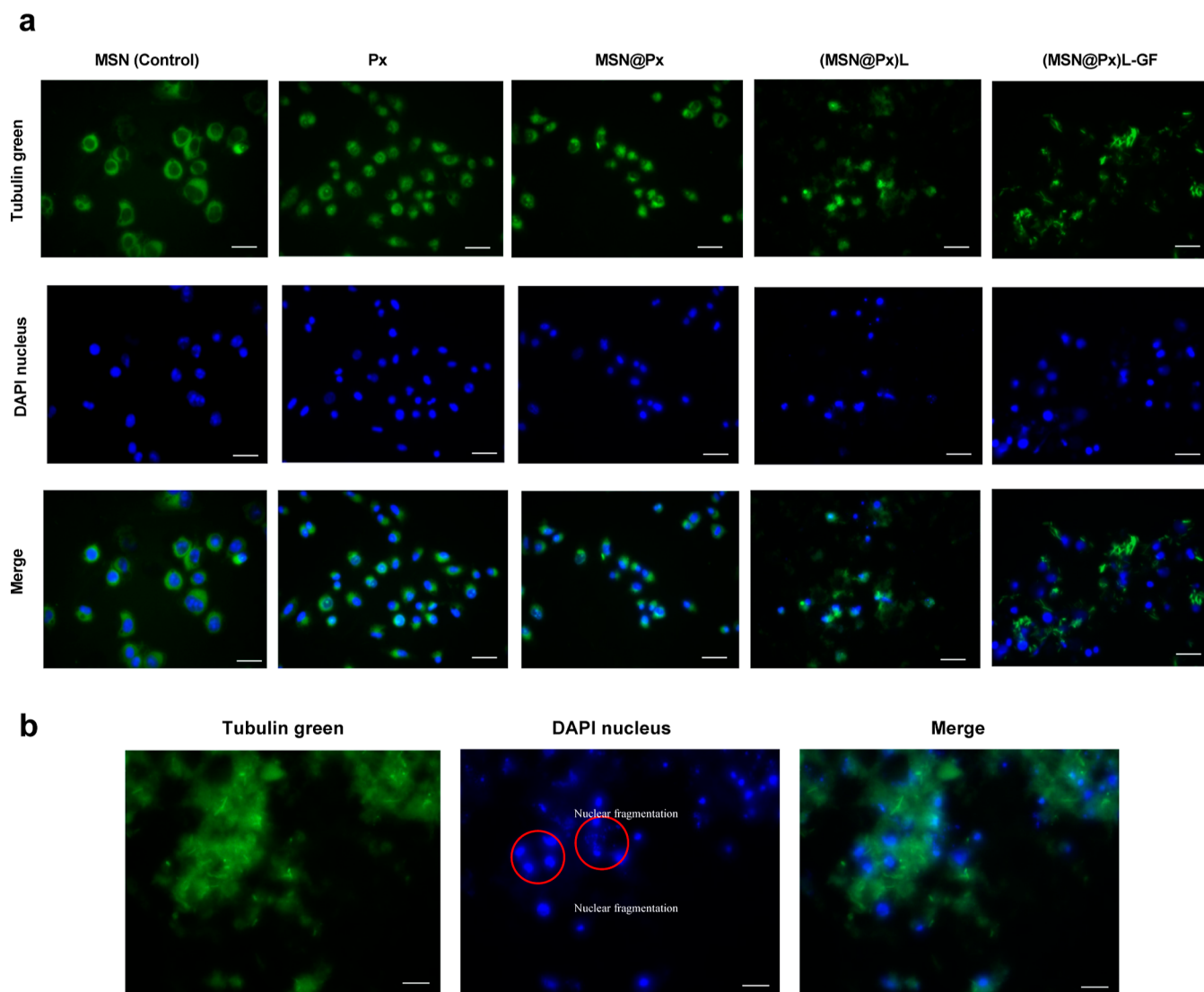
Figure 5. Fluorescence staining of tubulin and the nuclei of the A549 cells treated with the different nanoassemblies. The data are representative of three independent experiments (scale bar = 50 μm). (a) Assessment of the microtubule morphology after treatment with the nanoassemblies. (b) Scattered cytoskeleton with the fragmented and blebbed nuclei upon treatment with (MSN@Px) L-GF for 24 h.

in the A549 cells exposed to different nanoassemblies with equal encapsulated Px concentrations. Here, the conversion of a luciferin derivative to luciferin in the presence of GSH is determined using luminescence. As shown in Figure 4d, the GSH level in the MSNs was 5.99 ± 0.3 mM. The GSH content declined with the exposure to MSN@Px, (MSN@Px) L, and (MSN@Px) L-GF. Higher intracellular GSH levels in the MSNs have been related to apoptosis resistance, and it has been reported that the higher GSH levels are needed for tumor initiation and proliferation.[71,72] The GSH content in the presence of (MSN@PX) L-GF is as low as 1.4 ± 0.2 mM (Figure 4d). It has been reported that the GSH levels are reduced during oxidative stress.[72] This depletion of GSH levels indicates cell conditions close to apoptosis.[73]

To further demonstrate the apoptotic pathway mediated by the mitochondria, we tested the cellular ATP levels. The ATP levels of the A549 cells treated with the nanoassemblies were tested and compared with a known ATP series. The results from Figure 4e exhibited a significant loss of ATP levels with the (MSN@Px) L-GF. It showed up to 83.4, 76.7, 49.1, and 26.4% reduction of ATP for Px, Px@MSN, (MSN@Px) L, and

(MSN@Px) L-GF, respectively, when compared to a control (Figure 4e). Apoptosis requires energy since it is dependent on a few highly regulated processes involving a number of ATP-dependent steps, such as caspase activation, enzymatic hydrolysis of macromolecules, chromatin condensation, bleb formation, and apoptotic body formation.[74] These data indicate that the more damaged the mitochondria are, the less ATP they produce.

Taken together, the data from these assays of mitochondrial dysfunction confirm that the level of apoptosis is high with (MSN@Px) L-GF compared to that with the free drug, Px itself. These results verify that the mitochondrion-mediated apoptotic pathway is triggered by (MSN@Px) L-GF. Based on these results, we can conclude that the increase in the ROS levels (Figure 4b) induces ROS-triggered in situ mitochondrial damage (Figure 4c). This results in the decrease of the mitochondrial membrane potential (Figure 4c). The break-down of the mitochondria further amplifies the oxidative stress, decreasing the GSH levels (Figure 4d), which initiates cell death by consuming more intracellular ATP (Figure 4e).[10]
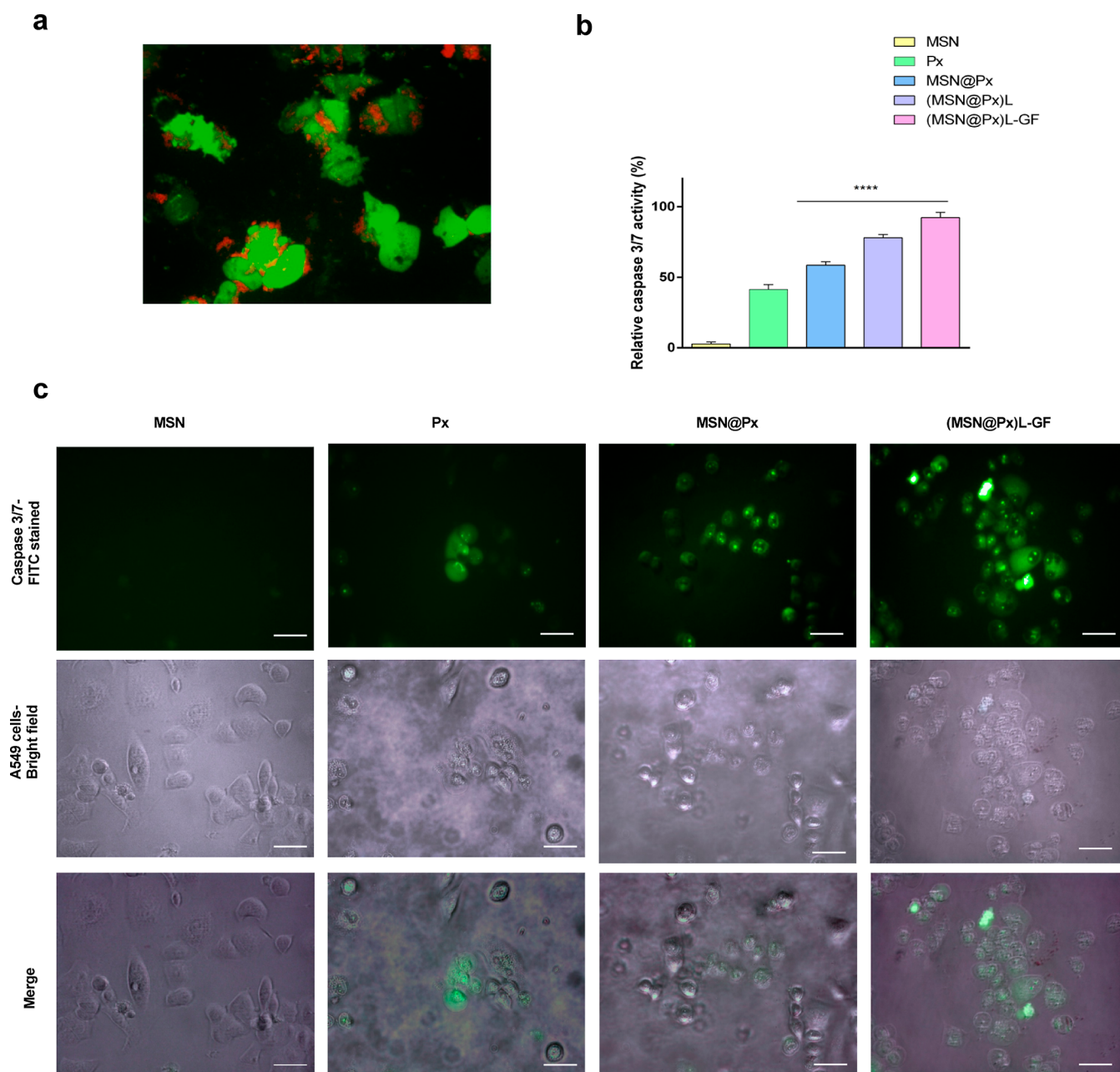
Figure 6. Analysis of apoptosis induction. (a) Morphological changes of the damaged A549 cells (green) upon treatment with (MSN@Px) L-GF (red). The cells are more distorted and changed their shape upon treatment. (b) Quantitative analysis of caspase 3/7 activity through a fluorometric assay. Data are presented as the mean ± SD (n = 3, **** indicates p < 0.0001) (c) Fluorescence microscopy images of caspase 3/7 activation in the A549 cells after treatment with different nanoassemblies (scale bar = 50 μm).

Detection of Microtubules Using Tubulin Assay. Assessment of the microtubule structure of the A549 cells following the nanoassembly treatment was used to further follow the apoptosis process (Figure 5). The microtubules are important structural components of the cytoskeleton. They are composed of polymerized α-tubulin and β-tubulin subunits organized to form protofilaments, which associate to form hollow cylindrical polymers of the microtubules. Taxanes, specially Px, are well-known microtubule-targeting agents that promote the disassembly of the microtubules.[75] Px can stabilize the microtubule polymers by binding to β-tubulin and inducing apoptosis by disrupting the dynamic remodeling of the microtubules during mitosis.[76,77]

As a result, monitoring Px and Px-loaded nanoassemblies for microtubule polymerization is essential to assess their anticancer activity (Figure 5). The microtubules were visualized by fluorescence microscopy using a fluorescent staining agent. This fluorescent agent is capable of permeating the live cells and staining the tubulin in the cells with green fluorescence.[78] Fine slender microtubule strands that resemble the cytoskeletal network covering the entire cytoplasmic area were clearly observed when the cells were treated with control MSNs (Figure 5a). However, when treated with (MSN@PX) L-GF, the cells clearly displayed a loss of the structured microtubular network with more scattered microtubules and condensed nuclei (Figure 5a,b). This demonstrates the ability of Px to disrupt the microtubular network. The more scattered
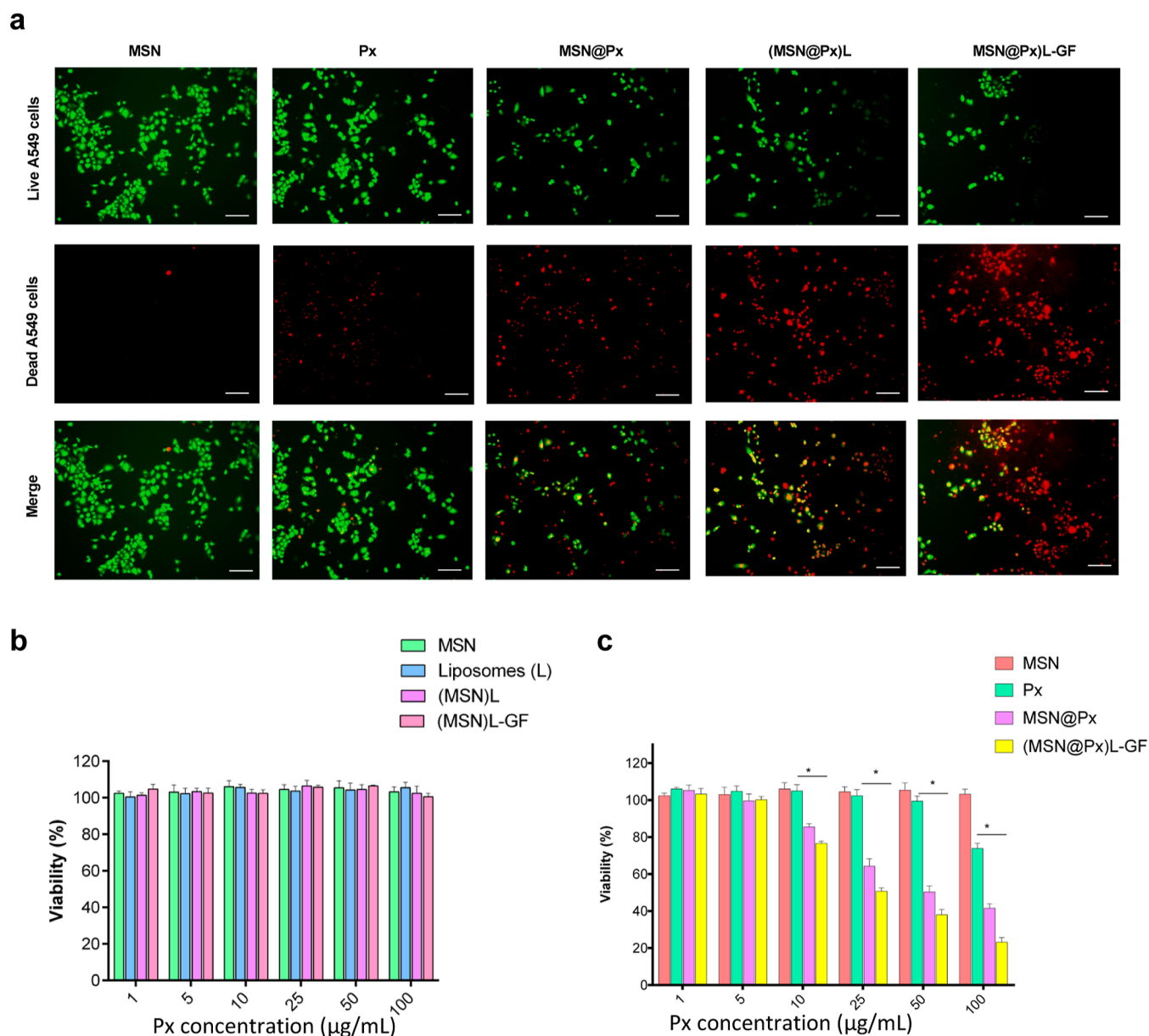
Figure 7. In vitro cytotoxicity analysis. (a) Fluorescence images of the A549 cells treated with different nanoassemblies. The live cells were stained with calcein AM, and the dead or apoptotic cells were stained with EthD-1 (scale bar = 50 μm). (b) Cell viability percentage of the A549 cells treated with different concentrations of different nanoassemblies for 12 h. (c) Cell viability percentage of the A549 cells treated with different concentrations of different nanoassemblies for 12 h. Data are presented as the mean ± SD ($n = 3$, * indicates $p < 0.05$).

tubular network that was observed in the cells treated with (MSN@PX) L-GF can be explained by the fact that the nanoassemblies were targeted properly and more Px is released from the targeted nanoassembly than by Px alone. Px (10 μg/mL treatment) led to greater thickening of the microtubule fibers compared to that by the control with only MSNs, which was indicated by a weaker green fluorescence in the cytoplasm. When comparing the cells treated with (MSN@Px) L-GF to those treated with MSN@Px, the nuclei became rounder in shape, indicating condensed nuclei, which suggests that apoptosis could be taking place (Figure 5).[77,79] Moreover, those cells showing condensed nuclei appeared had a tubulin structure that was completely collapsed and damaged, with a more scattered and disrupted surrounding, suggesting that these cells died from severe toxicity due to the inhibitory effects of (MSN@Px) L-GF in preventing microtubule

depolymerization (Figure 5b).[77,79] After 24 h of interaction with (MSN@Px) L-GF, the nuclei showed fragmentation, and the tubulin structure appeared to be more scattered and destroyed (Supporting Information Figure S9). Overall, the results indicate that the different nanoassemblies produced a qualitatively distinguishable tubulin structure.[77] This further validates the fact that (MSN@Px) L-GF is capable of delivering more Px to the A549 cells compared with the free drug, Px.

Assessment of Caspase 3/7 Activation. The next step was to evaluate the activation of caspase-3 and caspase-7 enzymes, which are key executioner enzymes in apoptosis (Figure 6).[80] Figure 6a clearly shows the A549 cell shrinkage and blebbing due to the interaction with our targeted nanoassembly. Direct visualization and quantification of apoptosis in the tumor cells have been utilized for assessing

the anticancer efficacy of the nanoassembly. Quantitative and qualitative expressions of caspase 3/7 activity were assessed to delineate the role of the effector caspase activity in the A549 cells in response to the nanoassemblies (Figure 6b,c). Caspase-3 (Cas-3) and caspase-7 (Cas-7) are cysteine−aspartic acid proteases, which can directly execute apoptosis followed after the sequential activation from activation of caspase-8 (Cas-8) or caspase-9 (Cas-9).[81] Activation of the caspases is the initial stage of the apoptotic process and is responsible for the cell changes during apoptosis, such as DNA fragmentation, nuclear chromatin condensation, and plasma membrane blebbing.[82] Thus, a Cas-3/7-specific cleavable peptide (DEVD) has been extensively used as a caspase-cleavable imaging probe for apoptosis imaging by monitoring caspase activity in the tumor cells in vitro and in vivo.[83]

This Cas-3/7 detection reagent is an intrinsically non-fluorescent dye as the DEVD peptide restricts the dye from binding to DNA. However, after the activation of Cas-3/7 in the apoptotic cells, the DEVD peptide is cleaved. This enables the dye to bind to DNA, producing bright green fluorescence.[84] This fluorescence can be observed using fluorescence microscopy and can be quantified at ~530 nm from a multiplate reader (Figure 6b). The results showed that the MSNs did not appear to activate Cas-3/7 in the A549 cells (Figure 6c). Strong Cas-3/7 activity was observed from MSN@Px and (MSN@Px) L-GF, as shown by the increased green fluorescence (Figure 6c). Furthermore, the increased cell blebbing and cell shrinkage from MSN@Px to (MSN@Px) L-GF also indicate apoptosis induction (Supporting Information Figure S10).[85] The Cas-3/7 activities for free Px and (MSN@Px) L-GF were 41.4 ± 3.5 and 92.4 ± 3.7% (Figure 6b), respectively. These data clearly suggest enhanced apoptotic induction in the presence of (MSN@Px) L-GF compared to that in the presence of free Px.

Synergistic Apoptosis and Cytotoxicity. As the collapsed tubulin structure resulted from the tubulin assay and the enhanced caspase activation observed from the caspase assay suggested the apoptotic activation, next, we evaluated the cancer cell viability via a live/dead cell viability assay. This cell viability assay can distinguish the live and the dead cells by simultaneously staining the live cells with green fluorescent calcein-AM, indicating intracellular esterase activity, and staining the dead cells with red fluorescent ethidium homodimer-1(EthD-1), indicating the loss of plasma membrane integrity.[86] The nanoassemblies having a Px equivalent of 10 μg/mL Px were incubated with the A549 cells for the assessment of their viability (Figure 7). As clearly observed from the figure, there is an increase in red fluorescence from the unloaded nanoparticles to (MSN@Px) L-GF, indicating an increase in the dead cells. The enhanced green fluorescence (more live cells) in MSNs indicates that the MSNs are nontoxic to the cells. Similarly, (MSN@Px) L-GF has effectively targeted the cancer cells and has efficiently delivered more drug, killing more cancer cells than that by the free drug, Px itself (Figure 7a). The MSNs, liposomes (LL), MSN@L, and MSN@L-GF exhibited low cytotoxicity against A549 at a concentration of 100 μg/mL (Figure 7b). To evaluate the cytotoxicity of the Px-loaded nanoassemblies, a standard series of MSN@Px, (MSN@Px) L, (MSN@Px) L-GF, and free Px having a Px concentration of 1, 5, 10, 25, 50, and 100 μg/mL were prepared and cultured with the A549 cells for 24 h. As shown in Figure 7c, the cells declined in viability with free Px, MSN@Px, (MSN@Px) L, and (MSN@Px) L-GF. Among the

nanoassemblies, (MSN@Px) L-GF showed enhanced cytotoxicity compared to free Px. At 10 μg/mL, (MSN@Px) L-GF showed 76.6 ± 1.2% viability, whereas the free drug Px had ~100% viability, indicating that almost all the cells are viable (Figure 7c). The in vitro antitumor effects of these nanoassemblies can be further quantitatively evaluated by IC_{50}, which is defined as the drug concentration at which 50% of the cells have been killed in a designated time period.[87] The 50% inhibiting concentration (IC_{50}) values for free Px, MSN@Px, and (MSN@Px) L-GF were calculated to be 59.2, 15.7, and 7.8 μg/mL of encapsulated Px, respectively (Supporting Information Figure S11). These results indicated that the IC_{50} value of the (MSN@Px) L-GF is 7.6 times lower than that of the free drug Px. So, (MSN@Px) L-GF is able to inhibit the A549 cells ~8× better than Px at the same concentration. The enhanced inhibition by (MSN@Px) L-GF is attributed (a) the dual-targeting ligands—which afford increased internalization, (b) the liposomal shell—which prevents premature drug release outside the cell, and (c) the mesoporous structure—which offered high loading of hydrophobic Px.[57,88]

■ DISCUSSION

In our study, liposome-coated MSNs were used to improve the efficacy of Px. Also, the FA and GE11 peptide conjugation with the MSN assembly was employed to decrease the internalization by the normal cells and enhance their targeting capability toward the tumor cells. Our findings demonstrate that the (MSN@Px) L-GF nanoassembly exhibited specific targeting toward the A549 cells, leading to the induction of cell apoptosis and cell cycle arrest. The obtained results show that the nanoassembly (MSN@Px) L-GF has a superior anticancer effect on the A549 cells with a 7.6 times lower value than that of free Px, while no notable toxicity was reported on the A549 cell line. In a previous in vitro study, Wang et al. reported the use of Px-loaded mesoporous nanoparticles for effective A549 therapy.[89] They have reported a 4.10-fold increased efficiency in Px-loaded mesoporous nanoparticles compared to that of the free drug, Px, in vitro.[89] This depicts the fact that the enhanced efficacy of our nanoassembly is due to the dual-targeting affinity and the controlled release of Px in the tumor vicinity due to the liposome coating.

Moreover, to achieve controlled drug release within the tumor microenvironment while minimizing the adverse effects on the normal tissues, the Px-loaded MSN was encapsulated within a liposome layer to address the poor solubility of PX and to restrict the premature release of Px. Another study reported a nanoassembly consisting of lipid-coated hollow mesoporous silica nanospheres (L-HMSNs) for codelivery of doxorubicin (DOX) and Px to synergistically inhibit the proliferation of A549 human lung cancer cells.[90] In this study, the drug-loading capacity for Px was reported as 4.5%.[90] In the present study, a high drug-loading efficiency of up to 24.5% was achieved using the core−shell MSN owing to their large pore size and high surface area. In addition, the results indicate that the targeted core−shell MSNs conjugated with FA and GE11 peptide could induce a higher apoptosis in the cells in comparison to that of the free drug itself. Based on the outcomes, our nanoassembly holds promising applications in the synergistic treatment of cancer and the development of new antitumor treatments exhibiting α-folate receptor over-expression. There is still need for some potential assessments such as in vivo targeting efficacy, tumor-inhibiting potential, and in vivo biocompatibility of the nanoparticles to investigate

the nanoparticles' capability to deliver various active substances and explore their therapeutic applications for treating different types of tumors. This comprehensive evaluation will provide valuable insights into the nanoparticles' performance and versatility, paving the way for their broader clinical applications in the field of cancer treatment.

CONCLUSIONS

In summary, we have successfully fabricated a very efficient dual-targeting nanoassembly (MSN@Px) L-GF as a delivery system for the hydrophobic anticancer drug, Px, for nonsmall lung carcinoma cells. (MSN@Px) L-GF has good stability, biocompatibility, and tumor-targeting capability via a folate receptor and an EGF receptor. (MSN@Px) L-GF also has a high clathrin-mediated endocytosis rate, controlled drug release in the acidic tumor environment, and ~8× increased efficacy compared to that of the free drug Px. After the treatment with (MSN@Px) L-GF, the cancer cells undergo apoptosis via the ROS-triggered mechanism. In situ mitochondrial damage leads to the amplification of oxidative stress and finally cell death. (MSN@Px) L-GF is a promising platform for anticancer drug delivery to improve the therapeutic efficacy of the anticancer drugs.

ASSOCIATED CONTENT

Ⓢ Supporting Information

The Supporting Information is available free of charge at https://pubs.acs.org/doi/10.1021/acsomega.3c02901.

> Additional experimental section; structure of Px and FA; calibration curve of FA and GE11 peptide; TEM image of bare liposome and liposome-coated MSN; FTIR comparison of CTAB and MSN; zeta potential of MSN@Px and (MSN@Px) L at 37 °C; surface area, pore volume, and pore size analysis of MSN and MSN@Px by BET; fluorescent image of nuclear fragmentation due to (MSN@Px) L-GF treatment; apoptosis study on the morphology of cells after treatment with MSN@Px and (MSN@Px) L-GF for 24 h; and normalized cancer cell viability (%) vs log Px concentration (mg/mL) (PDF)

AUTHOR INFORMATION

Corresponding Author

Unnati Patel − Department of Chemistry, The University of Alabama in Huntsville, Huntsville, Alabama 35899, United States; Ⓞ orcid.org/0000-0002-5117-2094; Phone: +1-2055677409; Email: up0004@uah.edu

Authors

Kavini Rathnayake − Department of Chemistry, The University of Alabama in Huntsville, Huntsville, Alabama 35899, United States

Emily C. Hunt − Department of Chemistry, The University of Alabama in Huntsville, Huntsville, Alabama 35899, United States

Nirupama Singh − Department of Chemistry, The University of Alabama in Huntsville, Huntsville, Alabama 35899, United States

Complete contact information is available at:
https://pubs.acs.org/10.1021/acsomega.3c02901

REFERENCES

(1) Bray, F.; Ferlay, J.; Soerjomataram, I.; Siegel, R. L.; Torre, L. A.; Jemal, A. Global cancer statistics 2018: GLOBOCAN estimates of incidence and mortality worldwide for 36 cancers in 185 countries. *Ca-Cancer J. Clin.* **2018**, *68* (6), 394−424.

(2) American Lung Association. *Lung cancer fact sheet*, 2018;.

(3) (a) Pisu, M.; Henrikson, N. B.; Banegas, M. P.; Yabroff, K. R. Costs of cancer along the care continuum: What we can expect based on recent literature. *Cancer* **2018**, *124* (21), 4181−4191. (b) Kaye, D. R.; Min, H. S.; Herrel, L. A.; Dupree, J. M.; Ellimoottil, C.; Miller, D. C. Costs of Cancer Care Across the Disease Continuum. *Oncologist* **2018**, *23* (7), 798−805.

(4) Chowdhury, M.; Sarkar, S.; Das, P. K. Photosensitizer Tailored Surface Functionalized Carbon Dots for Visible Light Induced Targeted Cancer Therapy. *ACS Appl. Bio Mater.* **2019**, *2* (11), 4953−4965.

(5) Cho, K.; Wang, X.; Nie, S.; Chen, Z.; Shin, D. M. Therapeutic Nanoparticles for Drug Delivery in Cancer. *Clin. Cancer Res.* **2008**, *14* (5), 1310−1316.

(6) Hui, Y.; Yi, X.; Hou, F.; Wibowo, D.; Zhang, F.; Zhao, D.; Gao, H.; Zhao, C.-X. Role of nanoparticle mechanical properties in cancer drug delivery. *ACS Nano* **2019**, *13* (7), 7410−7424.

(7) (a) Tran, S.; DeGiovanni, P.-J.; Piel, B.; Rai, P. Cancer nanomedicine: a review of recent success in drug delivery. *Clin. Transl. Med.* **2017**, *6* (1), 44. (b) Patel, U. S.Nanomaterials in Theranostics: Therapeutics and Diagnosis against Infectious DiseasesPh.D. ThesisThe University of Alabama in HuntsvilleAnn Arbor2022 (c) Patel, U.; Rathnayake, K.; Hunt, E. C.; Singh, N. Role of Nanomaterials in COVID-19 Prevention, Diagnostics, Therapeutics, and Vaccine Development. *J. nanotheranostics* **2022**, *3* (4), 151−176.

(8) (a) Patel, U.; Rathnayake, K.; Singh, N.; Hunt, E. C. Dual Targeted Delivery of Liposomal Hybrid Gold Nano-Assembly for Enhanced Photothermal Therapy against Lung Carcinomas. *ACS Appl. Bio Mater.* **2023**, *6*, 1915−1933. (b) Patel, U.; Hunt, E. C. Recent Advances in Combating Bacterial Infections by Using Hybrid Nano-systems. *Preprints* **2023**, 2023071941.

(9) Milkovic, L.; Cipak Gasparovic, A.; Cindric, M.; Mouthuy, P.-A.; Zarkovic, N. Short Overview of ROS as Cell Function Regulators and Their Implications in Therapy Concepts. *Cells* **2019**, *8* (8), 793.

(10) Zhang, W.; Hu, X.; Shen, Q.; Xing, D. Mitochondria-specific drug release and reactive oxygen species burst induced by polyprodrug nanoreactors can enhance chemotherapy. *Nat. Commun.* **2019**, *10* (1), 1704.

(11) (a) Jiang, H.; Zhang, X.-W.; Liao, Q.-L.; Wu, W.-T.; Liu, Y.-L.; Huang, W.-H. Electrochemical Monitoring of Paclitaxel-Induced ROS Release from Mitochondria inside Single Cells. *Small* **2019**, *15* (48), 1901787. (b) Perillo, B.; Di Donato, M.; Pezone, A.; Di Zazzo, E.; Giovannelli, P.; Galasso, G.; Castoria, G.; Migliaccio, A. ROS in cancer therapy: the bright side of the moon. *Exp. Mol. Med.* **2020**, *52* (2), 192−203. (c) Yu, Z.; Li, Q.; Wang, J.; Yu, Y.; Wang, Y.; Zhou, Q.; Li, P. Reactive Oxygen Species-Related Nanoparticle Toxicity in the Biomedical Field. *Nanoscale Res. Lett.* **2020**, *15* (1), 115.

(12) (a) Li, Z.; Barnes, J. C.; Bosoy, A.; Stoddart, J. F.; Zink, J. I. Mesoporous silica nanoparticles in biomedical applications. *Chem. Soc. Rev.* **2012**, *41* (7), 2590−2605. (b) Tang, F.; Li, L.; Chen, D. Mesoporous Silica Nanoparticles: Synthesis, Biocompatibility and Drug Delivery. *Adv. Mater.* **2012**, *24* (12), 1504−1534.

(13) Rathnayake, K.; Patel, U.; Pham, C.; McAlpin, A.; Budisalich, T.; Jayawardena, S. N. Targeted Delivery of Antibiotic Therapy to Inhibit Pseudomonas aeruginosa Using Lipid-Coated Mesoporous Silica Core-Shell Nanoassembly. *ACS Appl. Bio Mater.* **2020**, *3*, 6708−6721.

(14) Rathnayake, K. M. *Functionalized Nanomaterials as Tailored Theranostics*; The University of Alabama in Huntsville, 2022.

(15) Asefa, T.; Tao, Z. Biocompatibility of Mesoporous Silica Nanoparticles. *Chem. Res. Toxicol.* **2012**, *25* (11), 2265−2284.

(16) (a) Vivero-Escoto, J. L.; Slowing, I. I.; Trewyn, B. G.; Lin, V. S. Y. Mesoporous Silica Nanoparticles for Intracellular Controlled Drug Delivery. *Small* **2010**, *6* (18), 1952−1967. (b) Zhang, Q.; Liu, F.; Nguyen, K. T.; Ma, X.; Wang, X.; Xing, B.; Zhao, Y. Multifunctional Mesoporous Silica Nanoparticles for Cancer-Targeted and Controlled Drug Delivery. *Adv. Funct. Mater.* **2012**, *22* (24), 5144−5156. (c) Patel, U.; Rathnayake, K.; Jani, H.; Jayawardana, K. W.; Dhakal, R.; Duan, L.; Jayawardena, S. N. Near-infrared responsive targeted drug delivery system that offer chemo-photothermal therapy against bacterial infection. *Nano Sel.* **2021**, *2*, 1750−1769.

(17) (a) Moreira, A. F.; Dias, D. R.; Correia, I. J. Stimuli-responsive mesoporous silica nanoparticles for cancer therapy: A review. *Microporous Mesoporous Mater.* **2016**, *236*, 141−157. (b) Rahikkala, A.; Pereira, S. A. P.; Figueiredo, P.; Passos, M. L. C.; Araújo, A. R. T. S.; Saraiva, M. L. M. F. S.; Santos, H. A. Mesoporous Silica Nanoparticles for Targeted and Stimuli-Responsive Delivery of Chemotherapeutics: A Review. *Adv. Biosyst.* **2018**, *2* (7), 1800020. (c) Watermann, A.; Brieger, J. Mesoporous Silica Nanoparticles as Drug Delivery Vehicles in Cancer. *Nanomaterials* **2017**, *7* (7), 189.

(18) (a) Horwitz, S. B. Taxol (paclitaxel): mechanisms of action. *Ann. Oncol.* **1994**, *5*, S3. (b) Pazdur, R.; Kudelka, A. P.; Kavanagh, J. J.; Cohen, P. R.; Raber, M. N. The taxoids: paclitaxel (Taxol®) and docetaxel (Taxotere®). *Cancer Treat. Rev.* **1993**, *19* (4), 351−386. (c) Rowinsky, E. K.; Donehower, R. C. Paclitaxel (Taxol). *N. Engl. J. Med.* **1995**, *332* (15), 1004−1014.

(19) Markman, M.; Mekhail, T. M. Paclitaxel in cancer therapy. *Expert Opin. Pharmacother.* **2002**, *3* (6), 755−766.

(20) Ramalingam, S.; Belani, C. P. Paclitaxel for non-small cell lung cancer. *Expert Opin. Pharmacother.* **2004**, *5* (8), 1771−1780.

(21) Alexandre, J.; Hu, Y.; Lu, W.; Pelicano, H.; Huang, P. Novel Action of Paclitaxel against Cancer Cells: Bystander Effect Mediated by Reactive Oxygen Species. *Cancer Res.* **2007**, *67* (8), 3512−3517.

(22) Aggarwal, V.; Tuli, H. S.; Varol, A.; Thakral, F.; Yerer, M. B.; Sak, K.; Varol, M.; Jain, A.; Khan, M. A.; Sethi, G. Role of Reactive Oxygen Species in Cancer Progression: Molecular Mechanisms and Recent Advancements. *Biomolecules* **2019**, *9* (11), 735.

(23) Ma, P.; Mumper, R. J. Paclitaxel Nano-Delivery Systems: A Comprehensive Review. *J. Nanomed. Nanotechnol.* **2013**, *4* (2), 1000164.

(24) (a) Danhier, F.; Lecouturier, N.; Vroman, B.; Jérôme, C.; Marchand-Brynaert, J.; Feron, O.; Préat, V. Paclitaxel-loaded PEGylated PLGA-based nanoparticles: In vitro and in vivo evaluation. *J. Controlled Release* **2009**, *133* (1), 11−17. (b) Dong, Y.; Feng, S. S. Poly(d,l-lactide-co-glycolide)/montmorillonite nanoparticles for oral delivery of anticancer drugs. *Biomaterials* **2005**, *26* (30), 6068−6076. (c) Gao, Z.; Lukyanov, A. N.; Chakilam, A. R.; Torchilin, V. P. PEG-PE/phosphatidylcholine mixed immunomicelles specifically deliver encapsulated taxol to tumor cells of different origin and promote their efficient killing. *J. Drug Targeting* **2003**, *11* (2), 87−92. (d) He, M.; Zhao, Z.; Yin, L.; Tang, C.; Yin, C. Hyaluronic acid coated poly(butyl cyanoacrylate) nanoparticles as anticancer drug carriers. *Int. J. Pharm.* **2009**, *373* (1−2), 165−173. (e) Hu, F. Q.; Ren, G. F.; Yuan, H.; Du, Y. Z.; Zeng, S. Shell cross-linked stearic acid grafted chitosan oligosaccharide self-aggregated micelles for controlled release of paclitaxel. *Colloids Surf., B* **2006**, *50* (2), 97−103. (f) Karmali, P. P.; Kotamraju, V. R.; Kastantin, M.; Black, M.; Missirlis, D.; Tirrell, M.; Ruoslahti, E. Targeting of albumin-embedded paclitaxel nanoparticles to tumors. *Nanomedicine* **2009**, *5* (1), 73−82. (g) Kim, J. H.; Kim, Y. S.; Kim, S.; Park, J. H.; Kim, K.; Choi, K.; Chung, H.; Jeong, S. Y.; Park, R. W.; Kim, I. S.; et al. Hydrophobically modified glycol chitosan nanoparticles as carriers for paclitaxel. *J. Controlled Release* **2006**, *111* (1−2), 228−234. (h) Liang, H. F.; Chen, C. T.; Chen, S. C.; Kulkarni, A. R.; Chiu, Y. L.; Chen, M. C.; Sung, H. W. Paclitaxel-loaded poly(γ-glutamic acid)-poly(lactide) nanoparticles as a targeted drug delivery system for the treatment of liver cancer. *Biomaterials* **2006**, *27* (9), 2051−2059. (i) Lu, Z.; Yeh, T. K.; Tsai, M.; Au, J. L.; Wientjes, M. G. Paclitaxel-loaded gelatin nanoparticles for intravesical bladder cancer therapy. *Clin. Cancer Res.* **2004**, *10* (22), 7677−7684. (j) Mugabe, C.; Hadaschik, B. A.; Kainthan, R. K.; Brooks, D. E.; So, A. I.; Gleave, M. E.; Burt, H. M. Paclitaxel incorporated in hydrophobically derivatized hyperbranched polyglycerols for intra-vesical bladder cancer therapy. *BJU Int.* **2009**, *103* (7), 978−986. (k) Saravanakumar, G.; Choi, K. Y.; Yoon, H. Y.; Kim, K.; Park, J. H.; Kwon, I. C.; Park, K. Hydrotropic hyaluronic acid conjugates: Synthesis, characterization, and implications as a carrier of paclitaxel. *Int. J. Pharm.* **2010**, *394* (1−2), 154−161. (l) Sun, B.; Ranganathan, B.; Feng, S. S. Multifunctional poly(D,L-lactide-co-glycolide)/montmorillonite (PLGA/MMT) nanoparticles decorated by Trastuzumab for targeted chemotherapy of breast cancer. *Biomaterials* **2008**, *29* (4), 475−486. (m) Sun, T.-M.; Du, J.-Z.; Yao, Y.-D.; Mao, C.-Q.; Dou, S.; Huang, S. Y.; Zhang, P.-Z.; Leong, K.-W.; Song, E.-W.; Wang, J. Simultaneous delivery of siRNA and paclitaxel via a "two-in-one" micelleplex promotes synergistic tumor suppression. *ACS Nano* **2011**, *5* (2), 1483−1494. (n) Wang, J.; Mongayt, D.; Torchilin, V. P. Polymeric micelles for delivery of poorly soluble drugs: preparation and anticancer activity in vitro of paclitaxel incorporated into mixed micelles based on poly(ethylene glycol)-lipid conjugate and positively charged lipids. *J. Drug Targeting* **2005**, *13* (1), 73−80. (o) Xin, H.; Chen, L.; Gu, J.; Ren, X.; Wei, Z.; Luo, J.; Chen, Y.; Jiang, X.; Sha, X.; Fang, X. Enhanced anti-glioblastoma efficacy by PTX-loaded PEGylated poly(ε-caprolactone) nanoparticles: In vitro and in vivo evaluation. *Int. J. Pharm.* **2010**, *402* (1−2), 238−247. (p) Xin, H.; Jiang, X.; Gu, J.; Sha, X.; Chen, L.; Law, K.; Chen, Y.; Wang, X.; Jiang, Y.; Fang, X. Angiopep-conjugated poly(ethylene glycol)-co-poly(ε-caprolactone) nanoparticles as dual-targeting drug delivery system for brain glioma. *Biomaterials* **2011**, *32* (18), 4293−4305.

(25) Zhao, D.; Zhao, X.; Zu, Y.; Li, J.; Zhang, Y.; Jiang, R.; Zhang, Z. Preparation, characterization, and in vitro targeted delivery of folate-decorated paclitaxel-loaded bovine serum albumin nanoparticles. *Int. J. Nanomed.* **2010**, *5*, 669−677.

(26) (a) Dong, X.; Mattingly, C. A.; Tseng, M. T.; Cho, M. J.; Liu, Y.; Adams, V. R.; Mumper, R. J. Doxorubicin and paclitaxel-loaded lipid-based nanoparticles overcome multidrug resistance by inhibiting P-glycoprotein and depleting ATP. *Cancer Res.* **2009**, *69* (9), 3918−3926. (b) Ganta, S.; Amiji, M. Coadministration of Paclitaxel and curcumin in nanoemulsion formulations to overcome multidrug resistance in tumor cells. *Mol. Pharmaceutics* **2009**, *6* (3), 928−939. (c) Liu, Y.; Pan, J.; Feng, S. S. Nanoparticles of lipid monolayer shell and biodegradable polymer core for controlled release of paclitaxel: effects of surfactants on particles size, characteristics and in vitro performance. *Int. J. Pharm.* **2010**, *395* (1−2), 243−250. (d) Zhang, J. A.; Anyarambhatla, G.; Ma, L.; Ugwu, S.; Xuan, T.; Sardone, T.; Ahmad, I. Development and characterization of a novel Cremophor EL free liposome-based paclitaxel (LEP-ETU) formulation. *Eur. J. Pharm. Biopharm.* **2005**, *59* (1), 177−187.

(27) He, Y.; Liang, S.; Long, M.; Xu, H. Mesoporous silica nanoparticles as potential carriers for enhanced drug solubility of paclitaxel. *Mater. Sci. Eng., C* **2017**, *78*, 12−17.

(28) Wang, T.; Liu, Y.; Wu, C. RETRACTED ARTICLE: Effect of Paclitaxel-Mesoporous Silica Nanoparticles with a Core-Shell Structure on the Human Lung Cancer Cell Line A549. *Nanoscale Res. Lett.* **2017**, *12* (1), 66.

(29) Jia, L.; Shen, J.; Li, Z.; Zhang, D.; Zhang, Q.; Liu, G.; Zheng, D.; Tian, X. In vitro and in vivo evaluation of paclitaxel-loaded mesoporous silica nanoparticles with three pore sizes. *Int. J. Pharm.* **2013**, *445* (1−2), 12−19.

(30) Lin, J.; Cai, Q.; Tang, Y.; Xu, Y.; Wang, Q.; Li, T.; Xu, H.; Wang, S.; Fan, K.; Liu, Z.; et al. PEGylated Lipid bilayer coated mesoporous silica nanoparticles for co-delivery of paclitaxel and

curcumin: Design, characterization and its cytotoxic effect. *Int. J. Pharm.* **2018**, *536* (1), 272−282.

(31) (a) Jia, L.; Li, Z.; Shen, J.; Zheng, D.; Tian, X.; Guo, H.; Chang, P. Multifunctional mesoporous silica nanoparticles mediated co-delivery of paclitaxel and tetrandrine for overcoming multidrug resistance. *Int. J. Pharm.* **2015**, *489* (1−2), 318−330. (b) Liu, M.; Fu, M.; Yang, X.; Jia, G.; Shi, X.; Ji, J.; Liu, X.; Zhai, G. Paclitaxel and quercetin co-loaded functional mesoporous silica nanoparticles overcoming multidrug resistance in breast cancer. *Colloids Surf., B* **2020**, *196*, 111284.

(32) Yan, J.; Xu, X.; Zhou, J.; Liu, C.; Zhang, L.; Wang, D.; Yang, F.; Zhang, H. Fabrication of a pH/Redox-Triggered Mesoporous Silica-Based Nanoparticle with Microfluidics for Anticancer Drugs Doxorubicin and Paclitaxel Codelivery. *ACS Appl. Bio Mater.* **2020**, *3* (2), 1216−1225.

(33) Rana, S.; Shetake, N. G.; Barick, K. C.; Pandey, B. N.; Salunke, H. G.; Hassan, P. A. Folic acid conjugated Fe3O4 magnetic nanoparticles for targeted delivery of doxorubicin. *Dalton Trans.* **2016**, *45* (43), 17401−17408.

(34) Chen, D.-W.; Cheng, L.; Huang, F.; Cheng, L.; Zhu, Y.; Hu, Q.; Li, L.; Wei, L. GE11-modified liposomes for non-small cell lung cancer targeting: preparation, ex vitro and in vivo evaluation. *Int. J. Nanomed.* **2014**, *9*, 921−935.

(35) Genta, I.; Chiesa, E.; Colzani, B.; Modena, T.; Conti, B.; Dorati, R. GE11 Peptide as an Active Targeting Agent in Antitumor Therapy: A Minireview. *Pharmaceutics* **2017**, *10* (1), 2.

(36) Fernández, M.; Javaid, F.; Chudasama, V. Advances in targeting the folate receptor in the treatment/imaging of cancers. *Chem. Sci.* **2018**, *9* (4), 790−810.

(37) Hossein-Nejad-Ariani, H.; Althagafi, E.; Kaur, K. Small Peptide Ligands for Targeting EGFR in Triple Negative Breast Cancer Cells. *Sci. Rep.* **2019**, *9* (1), 2723.

(38) (a) Patel, K. Y.; Dedania, Z. R.; Dedania, R. R.; Patel, U. QbD approach to HPLC method development and validation of ceftriaxone sodium. *Future J. Pharm. Sci.* **2021**, *7* (1), 141. (b) Patel, R. B.; Patel, H. U.; Patel, U. Development and Validation of Stability Indicating RP-HPLC Method For the Estimation of Cabozantinib in Pharmaceutical Dosage Form. *Int. j. res. anal. rev.* **2020**, *7* (4), 892−907.

(39) Choi, Y. H.; Yoo, Y. H. Taxol-induced growth arrest and apoptosis is associated with the upregulation of the Cdk inhibitor, p21WAF1/CIP1, in human breast cancer cells. *Oncol. Rep.* **2012**, *28* (6), 2163−2169.

(40) LaBauve, A. E.; Rinker, T. E.; Noureddine, A.; Serda, R. E.; Howe, J. Y.; Sherman, M. B.; Rasley, A.; Brinker, C. J.; Sasaki, D. Y.; Negrete, O. A. Lipid-Coated Mesoporous Silica Nanoparticles for the Delivery of the ML336 Antiviral to Inhibit Encephalitic Alphavirus Infection. *Sci. Rep.* **2018**, *8* (1), 13990.

(41) Yang, S.; Han, X.; Yang, Y.; Qiao, H.; Yu, Z.; Liu, Y.; Wang, J.; Tang, T. Bacteria-Targeting Nanoparticles with Microenvironment-Responsive Antibiotic Release To Eliminate Intracellular Staphylococcus aureus and Associated Infection. *ACS Appl. Mater. Interfaces* **2018**, *10* (17), 14299−14311.

(42) Sercombe, L.; Veerati, T.; Moheimani, F.; Wu, S. Y.; Sood, A. K.; Hua, S. Advances and Challenges of Liposome Assisted Drug Delivery. *Front. Pharmacol* **2015**, *6* (286), Review.

(43) (a) Singh, R.; Kumar, C. S.; Banerjee, M.; Gupta, S. A Dual Drug Delivery Platform for Cancer-Bacteria Cotargeting. *ACS Appl. Bio Mater.* **2019**, *2* (11), 5032−5041. (b) Lu, Y.; Sega, E.; Leamon, C. P.; Low, P. S. Folate receptor-targeted immunotherapy of cancer: mechanism and therapeutic potential. *Adv. Drug Delivery Rev.* **2004**, *56* (8), 1161−1176. (c) Zwicke, G. L.; Mansoori, G. A.; Jeffery, C. J. Utilizing the folate receptor for active targeting of cancer nanotherapeutics. *Nano Rev.* **2012**, *3*, 18496. (d) Angelopoulou, A.; Kolokithas-Ntoukas, A.; Fytas, C.; Avgoustakis, K. Folic Acid-Functionalized, Condensed Magnetic Nanoparticles for Targeted Delivery of Doxorubicin to Tumor Cancer Cells Overexpressing the Folate Receptor. *ACS Omega* **2019**, *4* (26), 22214−22227.

(44) Yu, Y.; Wang, J.; Kaul, S. C.; Wadhwa, R.; Miyako, E. Folic Acid Receptor-Mediated Targeting Enhances the Cytotoxicity, Efficacy, and Selectivity of Withania somnifera Leaf Extract: In vitro and in vivo Evidence. *Front. Oncol.* **2019**, *9*, 602.

(45) Jayawardena, H. S. N.; Liyanage, S. H.; Rathnayake, K.; Patel, U.; Yan, M. Analytical Methods for Characterization of Nanomaterial Surfaces. *Anal. Chem.* **2021**, *93* (4), 1889−1911.

(46) Chu, Q.; Yuan, X.; Ji, W.; Chen, S.; Bao, Y.; Tan, S.; Lu, S.; Wu, K. A novel paclitaxel-loaded poly(d,l-lactide-co-glycolide)-Tween 80 copolymer nanoparticle overcoming multidrug resistance for lung cancer treatment. *Int. J. Nanomed.* **2016**, *11*, 2119−2131.

(47) Genta, I.; Chiesa, E.; Colzani, B.; Modena, T.; Conti, B.; Dorati, R. GE11 Peptide as an Active Targeting Agent in Antitumor Therapy: A Minireview. *Pharmaceutics* **2018**, *10* (1), 2.

(48) Kumar, N.; Salar, R. K.; Prasad, M.; Ranjan, K. Synthesis, characterization and anticancer activity of vincristine loaded folic acid-chitosan conjugated nanoparticles on NCI-H460 non-small cell lung cancer cell line. *Egypt. j. basic appl. sci.* **2018**, *5* (1), 87−99.

(49) Aisha, A. F.; Majid, A. M. S. A.; Ismail, Z. Preparation and characterization of nano liposomes of Orthosiphon stamineus ethanolic extract in soybean phospholipids. *BMC Biotechnol.* **2014**, *14*, 23.

(50) Martins, K. F.; Messias, A. D.; Leite, F. L.; Duek, E. A. R. Preparation and characterization of paclitaxel-loaded PLDLA microspheres. *Mater. Res.* **2014**, *17*, 650−656.

(51) (a) Jamshad, M.; Grimard, V.; Idini, I.; Knowles, T. J.; Dowle, M. R.; Schofield, N.; Sridhar, P.; Lin, Y.-P.; Finka, R.; Wheatley, M.; et al. Structural analysis of a nanoparticle containing a lipid bilayer used for detergent-free extraction of membrane proteins. *Nano Res.* **2015**, *8* (3), 774−789. (b) Li, Y.; Lin, J.; Yang, X.; Li, Y.; Wu, S.; Huang, Y.; Ye, S.; Xie, L.; Dai, L.; Hou, Z. Self-Assembled Nanoparticles Based on Amphiphilic Anticancer Drug-Phospholipid Complex for Targeted Drug Delivery and Intracellular Dual-Controlled Release. *ACS Appl. Mater. Interfaces* **2015**, *7* (32), 17573−17581.

(52) (a) Pi, J.; Jiang, J.; Cai, H.; Yang, F.; Jin, H.; Yang, P.; Cai, J.; Chen, Z. W. GE11 peptide conjugated selenium nanoparticles for EGFR targeted oridonin delivery to achieve enhanced anticancer efficacy by inhibiting EGFR-mediated PI3K/AKT and Ras/Raf/MEK/ERK pathways. *Drug Delivery* **2017**, *24* (1), 1549−1564. (b) Jiang, G.; Li, R.; Tang, J.; Ma, Y.; Hou, X.; Yang, C.; Guo, W.; Xin, Y.; Liu, Y. Formulation of Temozolomide-loaded nanoparticles and their targeting potential to melanoma cells. *Oncol. Rep.* **2017**, *37* (2), 995−1001.

(53) Varshosaz, J.; Hassanzadeh, F.; Sadeghi Aliabadi, H.; Nayebsadrian, M.; Banitalebi, M.; Rostami, M. Synthesis and Characterization of Folate-Targeted Dextran/Retinoic Acid Micelles for Doxorubicin Delivery in Acute Leukemia. *BioMed Res. Int.* **2014**, *2014*, 1−14.

(54) Lei, M.; Sha, S.; Wang, X.; Wang, J.; Du, X.; Miao, H.; Zhou, H.; Bai, E.; Shi, J.; Zhu, Y. Co-delivery of paclitaxel and gemcitabine via a self-assembling nanoparticle for targeted treatment of breast cancer. *RSC Adv.* **2019**, *9* (10), 5512−5520.

(55) Zhang, C.; Zhang, S.; Zhi, D.; Zhao, Y.; Cui, S.; Cui, J. Co-delivery of paclitaxel and survivin siRNA with cationic liposome for lung cancer therapy. *Colloids Surf., A* **2020**, *585*, 124054.

(56) Jiang, Y.; Zhou, Y.; Zhang, C. Y.; Fang, T. <p>Co-Delivery of Paclitaxel and Doxorubicin by pH-Responsive Prodrug Micelles for Cancer Therapy</p>. *Int. J. Nanomed.* **2020**, *15*, 3319−3331.

(57) Chen, M.; Hu, J.; Wang, L.; Li, Y.; Zhu, C.; Chen, C.; Shi, M.; Ju, Z.; Cao, X.; Zhang, Z. Targeted and redox-responsive drug delivery systems based on carbonic anhydrase IX-decorated mesoporous silica nanoparticles for cancer therapy. *Sci. Rep.* **2020**, *10* (1), 14447.

(58) (a) Lindner, L. H.; Hossann, M. Factors affecting drug release from liposomes. *Curr. Opin. Drug Discovery Dev.* **2010**, *13* (1), 111−123. (b) Wang, L. Preparation and in vitro evaluation of an acidic environment-responsive liposome for paclitaxel tumor targeting. *Asian J. Pharm. Sci.* **2017**, *12* (5), 470−477. (c) Huang, S.-T.; Wang, Y. P.;

Chen, Y.-H.; Lin, C.-T.; Li, W.-S.; Wu, H.-C. Liposomal paclitaxel induces fewer hematopoietic and cardiovascular complications than bioequivalent doses of Taxol. *Int. J. Oncol.* **2018**, *53* (3), 1105−1117.

(59) (a) Chang, C.-C.; Wu, M.; Yuan, F. Role of specific endocytic pathways in electrotransfection of cells. *Mol. Ther.–Methods Clin. Dev.* **2014**, *1*, 14058. (b) Sui, Z.-h.; Xu, H.; Wang, H.; Jiang, S.; Chi, H.; Sun, L. Intracellular Trafficking Pathways of Edwardsiella tarda: From Clathrin- and Caveolin-Mediated Endocytosis to Endosome and Lysosome. *Frontiers in Cellular and Infection Microbiology* **2017**, *7*, 400. (c) Chellan, B.; Reardon, C. A.; Getz, G. S.; Hofmann Bowman, M. A. Enzymatically Modified Low-Density Lipoprotein Promotes Foam Cell Formation in Smooth Muscle Cells via Macropinocytosis and Enhances Receptor-Mediated Uptake of Oxidized Low-Density Lipoprotein. *Arterioscler., Thromb., Vasc. Biol.* **2016**, *36* (6), 1101−1113.

(60) Bae, Y. S.; Oh, H.; Rhee, S. G.; Yoo, Y. D. Regulation of reactive oxygen species generation in cell signaling. *Mol. Cells* **2011**, *32* (6), 491−509.

(61) Manke, A.; Wang, L.; Rojanasakul, Y. Mechanisms of Nanoparticle-Induced Oxidative Stress and Toxicity. *BioMed Res. Int.* **2013**, *2013*, 1−15.

(62) Traverso, N.; Ricciarelli, R.; Nitti, M.; Marengo, B.; Furfaro, A. L.; Pronzato, M. A.; Marinari, U. M.; Domenicotti, C. Role of glutathione in cancer progression and chemoresistance. *Oxid. Med. Cell. Longevity* **2013**, *2013*, 1−10.

(63) He, H.; Lu, Y.; Qi, J.; Zhu, Q.; Chen, Z.; Wu, W. Adapting liposomes for oral drug delivery. *Acta Pharm. Sin. B* **2019**, *9* (1), 36−48.

(64) Alexandre, J.; Batteux, F.; Nicco, C.; Chéreau, C.; Laurent, A.; Guillevin, L.; Weill, B.; Goldwasser, F. Accumulation of hydrogen peroxide is an early and crucial step for paclitaxel-induced cancer cell death both in vitro and in vivo. *Int. J. Cancer* **2006**, *119* (1), 41−48.

(65) (a) Martínez-Carmona, M.; Colilla, M.; Vallet-Regí, M. Smart Mesoporous Nanomaterials for Antitumor Therapy. *Nanomaterials* **2015**, *5* (4), 1906−1937. (b) Murphy, M. P. How mitochondria produce reactive oxygen species. *Biochem. J.* **2009**, *417* (1), 1−13.

(66) Yoon, D. S.; Lee, M.-H.; Cha, D. S. Measurement of Intracellular ROS in Caenorhabditis elegans Using 2′,7′-Dichlorodi-hydrofluorescein Diacetate. *Bio-Protoc.* **2018**, *8* (6), No. e2774.

(67) Gogvadze, V.; Orrenius, S.; Zhivotovsky, B. Multiple pathways of cytochrome c release from mitochondria in apoptosis. *Biochim. Biophys. Acta* **2006**, *1757* (5−6), 639−647.

(68) Sivandzade, F.; Bhalerao, A.; Cucullo, L. Analysis of the Mitochondrial Membrane Potential Using the Cationic JC-1 Dye as a Sensitive Fluorescent Probe. *Bio-Protoc.* **2019**, *9* (1), No. e3128.

(69) Franco, R.; Cidlowski, J. A. Glutathione efflux and cell death. *Antioxid. Redox Signaling* **2012**, *17* (12), 1694−1713.

(70) Schieber, M.; Chandel, N. S. ROS function in redox signaling and oxidative stress. *Curr. Biol.* **2014**, *24* (10), R453−R462.

(71) Kennedy, L.; Sandhu, J. K.; Harper, M.-E.; Cuperlovic-Culf, M. Role of Glutathione in Cancer: From Mechanisms to Therapies. *Biomolecules* **2020**, *10* (10), 1429.

(72) Circu, M. L.; Yee Aw, T. Glutathione and apoptosis. *Free Radical Res.* **2008**, *42* (8), 689−706. PubMed.

(73) Ortega, A. L.; Mena, S.; Estrela, J. M. Glutathione in cancer cell death. *Cancers* **2011**, *3* (1), 1285−1310.

(74) (a) Kass, G. E.; Eriksson, J. E.; Weis, M.; Orrenius, S.; Chow, S. C. Chromatin condensation during apoptosis requires ATP. *Biochem. J.* **1996**, *318* (3), 749−752. (b) Hu, Y.; Benedict, M. A.; Ding, L.; Núñez, G. Role of cytochrome c and dATP/ATP hydrolysis in Apaf-1-mediated caspase-9 activation and apoptosis. *EMBO J.* **1999**, *18* (13), 3586−3595. (c) Zamaraeva, M. V.; Sabirov, R. Z.; Maeno, E.; Ando-Akatsuka, Y.; Bessonova, S. V.; Okada, Y. Cells die with increased cytosolic ATP during apoptosis: a bioluminescence study with intracellular luciferase. *Cell Death Differ.* **2005**, *12* (11), 1390−1397.

(75) Mukhtar, E.; Adhami, V. M.; Mukhtar, H. Targeting microtubules by natural agents for cancer therapy. *Mol. Cancer Ther.* **2014**, *13* (2), 275−284.

(76) Berges, N.; Arens, K.; Kreusch, V.; Fischer, R.; Di Fiore, S. Toward Discovery of Novel Microtubule Targeting Agents: A SNAP-tag-Based High-Content Screening Assay for the Analysis of Microtubule Dynamics and Cell Cycle Progression. *SLAS Discovery* **2017**, *22* (4), 387−398.

(77) Sum, C. S.; Nickischer, D.; Lei, M.; Weston, A.; Zhang, L.; Schweizer, L. Establishing a High-content Analysis Method for Tubulin Polymerization to Evaluate Both the Stabilizing and Destabilizing Activities of Compounds. *Curr. Chem. Genomics Transl. Med.* **2014**, *8* (1), 16−26.

(78) Inaba, H.; Yamamoto, T.; Iwasaki, T.; Kabir, A. M. R.; Kakugo, A.; Sada, K.; Matsuura, K. Fluorescent Tau-derived Peptide for Monitoring Microtubules in Living Cells. *ACS Omega* **2019**, *4* (6), 11245−11250.

(79) Yi, X.; Dai, J.; Han, Y.; Xu, M.; Zhang, X.; Zhen, S.; Zhao, Z.; Lou, X.; Xia, F. A high therapeutic efficacy of polymeric prodrug nano-assembly for a combination of photodynamic therapy and chemotherapy. *Commun. Biol.* **2018**, *1* (1), 202.

(80) Min, Y.; Li, J.; Liu, F.; Yeow, E. K.; Xing, B. Near-infrared light-mediated photoactivation of a platinum antitumor prodrug and simultaneous cellular apoptosis imaging by upconversion-luminescent nanoparticles. *Angew. Chem., Int. Ed. Engl.* **2014**, *53* (4), 1012−1016.

(81) Shim, M. K.; Yoon, H. Y.; Lee, S.; Jo, M. K.; Park, J.; Kim, J.-H.; Jeong, S. Y.; Kwon, I. C.; Kim, K. Caspase-3/-7-Specific Metabolic Precursor for Bioorthogonal Tracking of Tumor Apoptosis. *Sci. Rep.* **2017**, *7* (1), 16635.

(82) Sun, I.-C.; Lee, S.; Koo, H.; Kwon, I. C.; Choi, K.; Ahn, C.-H.; Kim, K. Caspase Sensitive Gold Nanoparticle for Apoptosis Imaging in Live Cells. *Bioconjugate Chem.* **2010**, *21* (11), 1939−1942.

(83) Shen, B.; Jeon, J.; Palner, M.; Ye, D.; Shuhendler, A.; Chin, F. T.; Rao, J. Positron Emission Tomography Imaging of Drug-Induced Tumor Apoptosis with a Caspase-Triggered Nanoaggregation Probe. *Angew. Chem., Int. Ed.* **2013**, *52* (40), 10511−10514.

(84) Odonkor, C. A.; Achilefu, S. Modulation of effector caspase cleavage determines response of breast and lung tumor cell lines to chemotherapy. *Cancer Invest.* **2009**, *27* (4), 417−429.

(85) Ma, D.-D.; Yang, W.-X. Engineered nanoparticles induce cell apoptosis: potential for cancer therapy. *Oncotarget* **2016**, *7* (26), 40882−40903.

(86) Bourke, S.; Mason, H. S.; Borok, Z.; Kim, K. J.; Crandall, E. D.; Kemp, P. J. Development of a lung slice preparation for recording ion channel activity in alveolar epithelial type I cells. *Respir. Res.* **2005**, *6* (1), 40.

(87) W Caldwell, G.; Yan, Z.; Lang, W.; A Masucci, J. The IC(50) concept revisited. *Curr. Top. Med. Chem.* **2012**, *12* (11), 1282−1290.

(88) Wang, T.; Liu, Y.; Wu, C. Effect of Paclitaxel-Mesoporous Silica Nanoparticles with a Core-Shell Structure on the Human Lung Cancer Cell Line A549. *Nanoscale Res. Lett.* **2017**, *12* (1), 66.

(89) Wang, T.; Liu, Y.; Wu, C. Effect of paclitaxel-mesoporous silica nanoparticles with a core-shell structure on the human lung cancer cell line A549. *Nanoscale Res. Lett.* **2017**, *12*, 66.

(90) Qiu, Y.; Wu, C.; Jiang, J.; Hao, Y.; Zhao, Y.; Xu, J.; Yu, T.; Ji, P. Lipid-coated hollow mesoporous silica nanospheres for co-delivery of doxorubicin and paclitaxel: preparation, sustained release, cellular uptake and pharmacokinetics. *Mater. Sci. Eng., C* **2017**, *71*, 835−843.